Journal of Fluids and Structures 106 (2021) 103353

Contents lists available at ScienceDirect

Journal of Fluids and Structures

journal homepage: www.elsevier.com/locate/jfs

Bag and floater motions of a fabric membrane cage

Muhammad Mukhlas [a,*], Pål Furset Lader [a], David Kristiansen [a], Trygve Kristiansen [a], Motoyasu Kanazawa [b]

[a] Department of Marine Technology, Norwegian University of Science and Technology, Trondheim, Norway
[b] Department of Ocean Operations and Civil Engineering, Norwegian University of Science and Technology, Ålesund, Norway

ARTICLE INFO

Article history:
Received 10 December 2020
Received in revised form 6 June 2021
Accepted 6 August 2021
Available online 26 August 2021

Keywords:
Aquaculture
Hydroelasticity
Gravity waves
Membrane structures
Model-scale experiment
Fluid–structure interaction

ABSTRACT

We investigate bag and floater motions of a scaled fabric membrane cage model. Model tests with an assumed model scale of 1:27 were performed at SINTEF Ocean's towing tank, where the cage model consisted of an enclosing fabric (or a bag), an elastic floater, a mooring system, and an internal water mass. The model was moored in a towing tank and subjected to regular waves with different periods and steepnesses. The first harmonic component of the floater and bag motions time series were analyzed, and image analysis was performed for the latter. Several interesting responses of the fabric membrane cage are discussed: cage set-down, wavelike bag motion, and floater motions. The magnitude of the cage set-down is dependent on the incident wave period and steepness; the magnitude increases in response to a longer and steeper wave. The bag also exhibits a wavelike motion that propagates from the floater to the bottom part of the cage and has apparent implications for the dynamics of the bag bottom and the snap loads on the fabric material. Simplified numerical simulations were performed using WAMIT, which assumed a rigid cage model. A floater motions comparison between model tests and WAMIT results shows the importance of taking the bag and floater flexible modes into account when performing hydrodynamic analysis of a fabric membrane cage.

1. Introduction

The concept of a bio-secure aquaculture structure has in recent years gained traction in the Norwegian aquaculture industry. Net-based cages currently produce most of the farmed salmon in Norway. However, net cages have problems with salmon lice, escapes, and the spread of pollutants, which highlights a need for more sustainable technologies for industrial development. Floating closed containment systems (or closed cages) are one of many viable solutions. Closed cages isolate the water volume inside the cage with impermeable materials. Sensors and a water exchange system allow farmers better control over the water quality inside the cage, resulting in less environmental impact and protection against salmon lice, as water intake can be pumped from a water depth with smaller populations of sea lice. At the same time, the sedimentable particles and dead salmon can be collected from the cages' outlets and pumped to the surface (Nilsen et al., 2017). Multiple pumps are used to artificially circulate water inside the cage, where the velocity is regulated to optimize salmon growth rates and welfare (Nilsen et al., 2019). However, in spite of all the benefits associated with closed cages, there is limited experience operating such cages, especially at exposed locations with significant waves.

* Corresponding author.
E-mail address: muhammad.mukhlas@ntnu.no (M. Mukhlas).

https://doi.org/10.1016/j.jfluidstructs.2021.103353

Regarding the hydrodynamic characteristics of closed and net cages, there are distinct differences that are worth mentioning here. Firstly, closed cages' internal water mass must be accounted for in dynamic conditions, yielding a higher effective mass than that of net cages by a thousandfold. Therefore, closed cages represent large volume structures from a hydrodynamic perspective and behave differently in waves than the net cages do. In addition, slowly-varying and mean wave forces are important for a large volume structure, and their effects must be taken into account in mooring system design. Secondly, the presence of free-surface inside a closed cage introduces sloshing (Ibrahim, 2006; Faltinsen and Timokha, 2009), a resonance phenomenon of standing wave modes in confined/semi-confined liquid with a free surface. Sloshing is excited by the body's motions, which in return has a significant influence on the motions themselves and on mean wave forces (Newman, 2005). Lastly, the artificial water circulation inside the cage will alter sloshing and its hydrodynamic pressure contribution and consequently modify the cage behavior in the wave. A slowly rotating liquid with uniform angular velocity and forced horizontal oscillation was found to modify the sloshing regimes of a non-rotating liquid by splitting the natural frequencies (Tsarau et al., 2021).

Several concepts of closed cages have been tested in Norway, where they typically differ in sizes (e.g., 2500–21000 m^3) and geometrical shapes (e.g., ellipsoidal, rectangular, and cylindrical). A closed cage typically comprises a floater, a mooring system, and an impermeable cage. Based on the load-carrying characteristics, closed cages can be categorized into:

1. Rigid cages (e.g., concrete and steel).
2. Elastic cages (e.g., glass-reinforced plastic (GRP)). Limited material stiffness used to restrain compression, tension forces, and bending moments.
3. Fabric membrane cages (e.g., Polyvinyl chloride (PVC) tarpaulin). Fabric provides negligible bending and compressive stiffness.

The categorization suggests different structural modeling for the hydrodynamic analysis, and consequently, the seakeeping behavior differs from one category to another. Only a few published studies on the interaction between floating closed cages and waves or currents are available. Numerical and experimental study of rigid cage responses and mooring forces in regular waves was presented in Kristiansen et al. (2018b); it was found that sloshing had a significant influence on both cage responses and mean wave force. Tan et al. (2019) numerically investigated the coupled motion of a rigid circular cylinder cage in regular waves, paying special attention to nonlinear swirling of the internal fluid. Significant swirling was found in the vicinity of the lowest antisymmetric sloshing frequency. Comparison between quasi-static and fully coupled hydroelastic analyses on the stress of a two-dimensional elastic cage was studied numerically in Strand and Faltinsen (2020). Within their studied wave frequency range and examined stiffnesses, the study revealed that the quasi-static assumption in structural stress calculation was conservative with respect to the fully coupled hydroelastic analysis, excepting those frequencies very close to the lowest symmetric sloshing frequency. Studies involving fabric membrane cages have focused on investigation of drag forces (Strand et al., 2013, 2014; Lader et al., 2015; Strand et al., 2016) and on wave responses (Lader et al., 2017; Strand and Faltinsen, 2019). The influence of cage filling and membrane behavior on the drag force and wave responses were emphasized in these studies. In addition, it was reported in Solaas et al. (1993) and Lader et al. (2017) that the fabric showed an interesting wavelike membrane motion that propagates from the floater to the bottom part of the cage. Such motion, which can potentially create large snap loads within the fabric, was also observed in the present model tests.

There is only a modest amount of literature on ocean structures in gravity waves in which the membrane is the main constituent of the constructions. These include fluid-filled membrane breakwater (Ohyama et al., 1989), flexible membrane wave barrier (Thompson et al., 1992), and floating fluid-filled membrane barge (Hawthorne, 1961). Prior to hydrodynamic analysis of such structures, their unknown static configurations must be found iteratively from the equilibrium of self-weight, static fluid pressure, and tensile loads acting on the structures (e.g., Hawthorne (1961), Løland and Aarsnes (1994), Zhao and Triantafyllou (1994), Phadke and Cheung (1999) and Strand (2018)). The hydrodynamic problem can then be formulated using potential flow theory (for instance) for the fluid domains, for which the kinematic and dynamic conditions on the membrane must be satisfied. Depending on its static configuration, the dynamic condition on the membrane can be formulated using tensioned string model (Kim et al., 1996; Kim and Kee, 1996; Kee and Kim, 1997; Cho and Kim, 1998; Lo, 2000; Lee and Lo, 2002), lumped mass–spring model (Ohyama et al., 1989; Tanaka et al., 1990, 1992), planar cable model (Zhao, 1995; Zhao and Aarsnes, 1998; Strand and Faltinsen, 2019), and membrane theory of thin cylindrical shells model (Phadke and Cheung, 1999). Both velocity potentials and membrane motion need to be solved simultaneously. Most of the literature above assumed two-dimensional linear problems on their fluid flow and membrane dynamic formulations, which are only valid for small incident wave and membrane motion amplitudes. In addition, dynamic tension along the membrane is required to be smaller than the pretension, and this may only be valid on a certain range of static configuration and wave conditions (Zhao, 1995; Strand and Faltinsen, 2019).

When a small membrane deformation assumption does not hold, a geometrically nonlinear model of the membrane is required (Broderick and Leonard, 1992). Broderick and Leonard (1992, 1995) presented a nonlinear boundary element model (BEM) coupled with a nonlinear finite element model (FEM) of the membrane in time-domain; they investigated the interaction of highly deformable fluid-filled submerged cylindrical membranes and gravity waves with their published experimental results (Broderick and Jenkins, 1993). Discrepancies between their experimental and numerical results can be explained by the constant internal pressure assumption of their numerical model, and they emphasized the importance of including a BEM model of the internal fluid. Phadke and Cheung (2003), to further study the experimental results of

Table 1
Summary of structural properties that were used in model tests. Full-scale values are given for reference.

Description	Symbols	Model scale	Full scale (1:27)
Cage total mass in air (excl. internal water mass)	M_{bag}	$<$ 3 kg	$<$ 59.05 tonnes
Fabric cage properties			
Cage diameter	D_{bag}	1.5 m	40.5 m
Cage draught	h_{bag}	0.75 m	20.25 m
Cage freeboard	f_{bag}	8 cm	2.16 m
Elastic moduli	E_{avg}	443 MPa	–
Floater properties			
Pipe diameter	$2c$	16 mm	0.432 m
Floater diameter	$D_{fl} = D_{bag} + 4c$	1.532 m	41.364 m
Floater bending stiffness	EI_{fl}	4.1 10^{-2} N m^2	5.9 10^5 N m^2
Mooring lines properties			
Coil spring stiffness	k_s	90 N/m	65.61 kN/m
Spring yield limit	$f_{y,s}$	120 N	2361.96 kN/m
Mooring line pretension	$T_{0,m}$	40 N	787.32 kN/m

fluid-filled membrane breakwater in Ohyama et al. (1989), considered a coupled nonlinear FEM and linear BEM for the fluids flows. Their numerical results showed the importance of the membrane's geometric nonlinearity even for relatively small wave steepness and membrane response amplitude. Nonlinear membrane response characteristics, such as higher harmonic components, steady hoop tension, strain stiffening, and hysteresis, were apparent from their results, which were more prominent for increasing wave steepness and decreasing constant internal pressure.

This study presents physical model test results of a half-spherical fabric membrane cage in regular waves. All of the studies on fluid-filled membrane structures that were cited above showed significant interactions between membrane deformations with external and internal fluid flows. Similarly, significant coupling effects between floater, membrane, and internal fluid responses influenced the fabric membrane cage seakeeping behavior in waves. Possible significant interaction of the membrane and floater motions are addressed. Cage set-down under incident wave forces was observed in the model tests, and the analysis results are presented. In addition, challenges encountered in model tests are expressed and discussed.

The paper is organized as follows: the model tests are discussed in Section 2. Section 3 presents all the results and findings from model tests followed by their discussions. Lastly, the conclusions are given in Section 4.

2. Model tests

2.1. Experimental setup

A schematic drawing of the experimental setup is given in Fig. 1. Physical model tests of a fabric membrane cage were conducted at SINTEF Ocean's towing tank in Trondheim, Norway. The tests were intended to experimentally investigate the behavior of closed cages in waves and were a part of a larger project called SJØFLO (Kristiansen et al., 2018a). The towing tank dimension was 85 m long, 10.5 m wide, and 10 m deep. The regular waves were generated by a double flap-type wavemaker installed at one of the tank ends and were damped by a parabolic beach installed at the other end. The tests were conducted by assuming Froude scaling with model scale of 1:27.

2.1.1. The model

The model consisted of an enclosing fabric (or a bag), an elastic floater, a mooring system, and an internal water mass. The structural properties of the model are summarized in Table 1. The bag was filled with freshwater until the floater was approximately half-submerged, so the water volume was only visually maintained. The bag was slightly overfilled at the beginning of the model tests; the filling level was approximately 100.1% of the theoretical half-sphere volume. The filling level was estimated by equating the displaced water volume of a half-submerged floater with the overfilling volume and by assuming a negligible bag mass. Therefore, the difference between the water level inside and outside of the bag was approximately 5 mm. A generic geometrical bag shape was considered, and a half-sphere shape was chosen. We decided to neglect internal structures (e.g., pumps, pipes, outlets, and nets) to minimize the modeling complexity. With the assumed scale factor, the full-scale dimension of the model would be comparable to some existing fabric membrane cages. However, the chosen parameters within the present study were not intended to represent any particular existing fabric membrane cages.

A waterproof parachute fabric (0-P) similar to that used by Kristiansen et al. (2018c) was chosen as the bag material. The fabric was an anisotropic material; the directional averaged Young's modulus value E_{avg} is given in Table 1. Eight fabric sheets were sewn together with wool threads to form a half-spherical bag. For a correct model scaling of the fabric

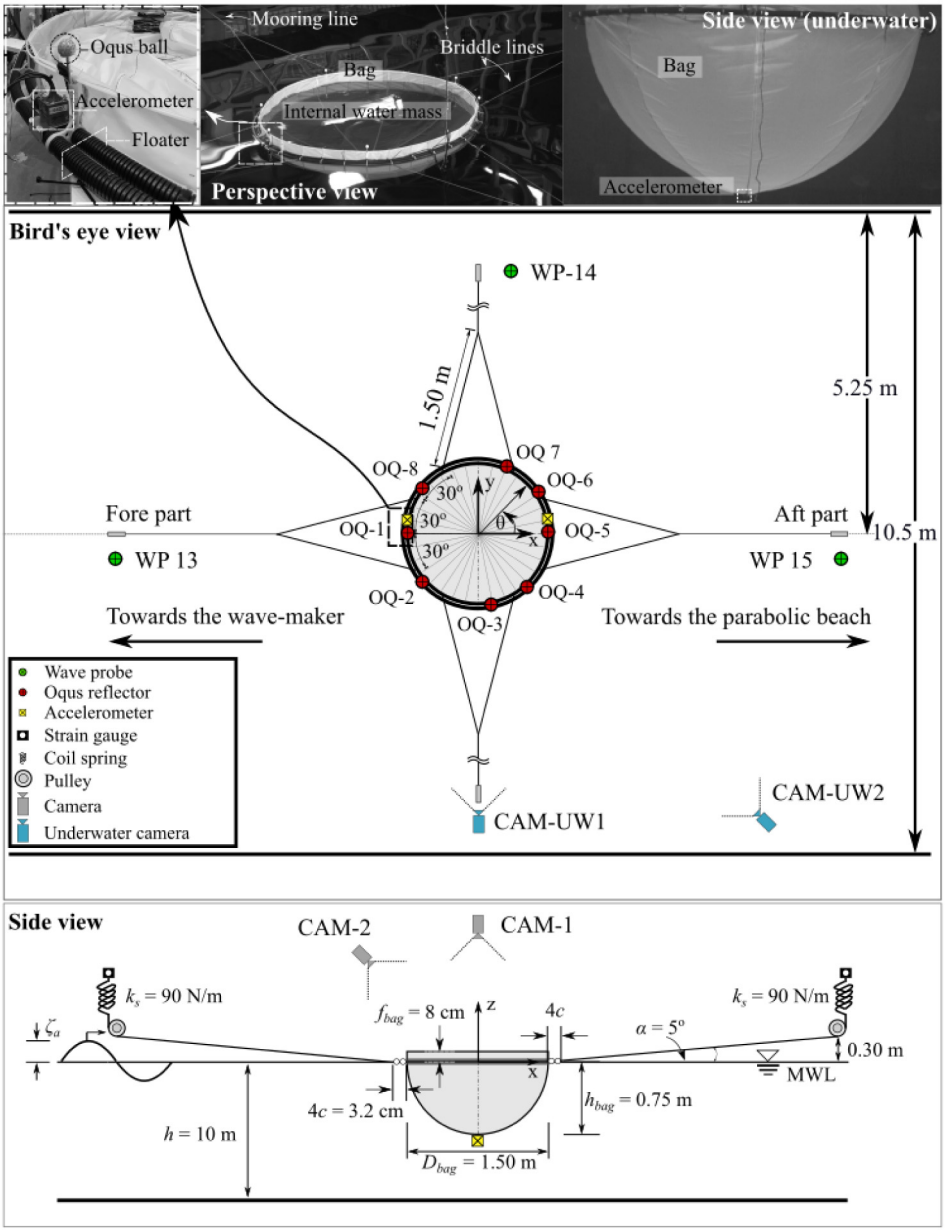

Fig. 1. Schematic drawing (not to scale) of the experimental setup. Photos from the model tests are in the upper portion. The middle is a bird's eye view, and the lower is a side view. A right-handed coordinate system is located at the center of the floater at the mean water level (MWL).

membrane cage in gravity waves, a similar Froude number and non-dimensionalized parameter $E\ d\ /\ \rho\ g\ L^2$ are required for both model and full scale (Faltinsen and Shen, 2018; Strand and Faltinsen, 2019). E, d, ρ, g, and L are Young's modulus, membrane thickness, water density, gravitational acceleration, and characteristic cage length, respectively. Due to similar ρ and g values on both scales, one can only adjust the $E\ d$ value to determine the fabric material in the model scale. However, such fabric material does not exist for typical model scales, and this may result in an "elasticity-error" effect on the response of the model (Strand and Faltinsen, 2019). Therefore, we instead chose a widely-available waterproof material with negligible bending and compressive stiffnesses.

The bag rim was attached to the floater using 32 connectors installed along the circumference. One of these connectors is portrayed in Fig. 1 (picture on the upper-left, below the Oqus ball). The floater, modeled by two flexible electrical conduits made of PVC, was inspired by the typical floatation system of net cages. The typical full-scale values of double-space HDPE pipe with an outer diameter of 0.5 m are $E\ I_x = 2.31\ 10^6$ N m^2 and $E\ I_z = 1.97\ 10^7$ N m^2 (Lader et al., 2017). The $E\ I_x$ value was considered representative for typical full scale, as one can find a factor of 20 of $E\ I_x$ values between

Table 2
Overview of the regular wave cases used in the model tests. Left: The model scale values of the used wave parameters. Right: wave classifications according to NS9415 (2009). Classifications in the left table are calculated based on geometrical similarity with the assumed model scale of 1:27.

T (s)	λ (m)	λ / D_{bag}	Wave height H (cm)		
			ε = 1/60	ε = 1/45	ε = 1/30
0.69	0.74	0.49	1.24	1.65	2.47
0.74	0.87	0.58	1.44	1.92	2.89
0.75	0.89	0.59	1.48	1.97	2.96
0.84	1.11	0.74	1.85	2.47	3.70
0.85	1.14	0.76	1.90	2.53	3.80
0.97	1.48	0.99	2.47	3.29	4.94
0.99	1.54	1.03	2.57	3.42	5.13
1.03	1.67	1.11	2.78	3.71	5.56
1.09	1.85	1.24	3.09	4.12	6.18
1.27	2.52	1.68	4.20	5.60	
1.30	2.64	1.76	4.40	5.87	
1.38	2.96	1.98	4.94	6.59	
1.45	3.29	2.19	5.48	7.31	
1.49	3.47	2.32	5.79	7.72	
1.54	3.70	2.47	6.17		
1.69	4.45	2.97	7.41	9.88	
1.69	4.46	2.97	7.43		
1.82	5.19	3.46	8.64		
1.95	5.92	3.95	9.87		
2.02	6.35	4.23	10.59		
2.09	6.79	4.53	11.32		
2.32	8.37	5.58	13.95		
2.48	9.64	6.43	16.06		

NS9415:2009 Wave classifications (H = 1.9 H_s)					
Small			H	<	1.0 m
Moderate	1.0 m	<	H	<	1.9 m
Medium	1.9 m	<	H	<	3.8 m
High	3.8 m	<	H	<	5.7 m
Extreme	5.7 m	<	H		

the stiffest and the most flexible commercial HDPE floater. A much lower full-scale value of $E\ I_z$ in the floater model was not considered to be critical since the mooring lines maintained the horizontal shape.

The cage was steadied, in both in-line and transverse directions, by crowfoot mooring lines. High-stiffness multi-filament lines were used for both mooring and bridle lines material, while the mooring line stiffness was modeled by a coil spring. Pretension was applied equally to all the mooring lines to avoid slack during the tests. The mooring lines were elevated as depicted in Fig. 1 to avoid contact with the waves during the tests. Hence, the distance between the cage center and the pulleys and wave probes was approximately $0.5\ D_{bag} + 4c + \{0.30\ /\ \tan\ \alpha\} = 4.21$ m.

2.1.2. The instrumentation

Sensors, cameras, and other components of the setup are illustrated by the given symbols in Fig. 1. The sensors consisted of strain gauges in the four mooring lines, three capacitance wave probes, three 2 g accelerometers, and a motion-tracking optical system Qualisys Oqus. In addition, four 50 fps cameras were used to record videos from the tests. All the sensors and cameras acquired the data synchronously, and all data were logged with the same reference clock. The sensors' signals were acquired at a sampling frequency of 200 Hz.

The Oqus system was used to track displacement of several points along the floater in time. Eight Oqus balls were distributed along the inner floater circumference, which in equilibrium can be described by $m_{i,0} = [r_{i,0}, \theta_{i,0}, z_{i,0}]$, where i = 1, 2, .., 8. Theoretically, the radial position of each ball was $r_{i,0} = 0.75$ m in correspondence with the bag radius. The circumferential and vertical positions of the balls were $\theta_{i,0} = [180°\ ,\ 222°\ ,\ 278°\ ,\ 306°\ ,\ 0°\ ,\ 29°\ ,\ 70°\ ,\ 112°\ ]$ and $z_{i,0} =$ [0.109, 0.106, 0.104, 0.095, 0.111, 0.123, 0.103, 0.111] meters, respectively. The instantaneous position of the balls $m_i(t) = [x_i(t), y_i(t), z_i(t)]$ were tracked from camera images by means of triangularization. The measured position on each ball can be related to the rigid and elastic perturbation modes of the circular floater by means of a Fourier series, which can be expressed as:

$$\begin{aligned} x_i(\theta, t) &= \eta_1(t) + x_{i,0}(\theta, t) + \nu(\theta, t)\ \cos\ \theta \\ y_i(\theta, t) &= \eta_2(t) + y_{i,0}(\theta, t) + \nu(\theta, t)\ \sin\ \theta \\ z_i(\theta, t) &= \sum_{n=0}^{\infty} a_n(t)\ \cos\ n\theta \end{aligned} \tag{1}$$

where

$$\begin{aligned} x_{i,0}(\theta,\ t) &= r_{i,0}(\theta,\ 0)\ \cos\ \theta \quad \text{(initial x-position)} \\ y_{i,0}(\theta,\ t) &= r_{i,0}(\theta,\ 0)\ \sin\ \theta \quad \text{(initial y-position)} \\ \nu(\theta,\ t) &= \sum_{n=2}^{\infty} b_n(t)\ \cos\ n\theta \quad \text{(radial deflection)} \end{aligned} \tag{2}$$

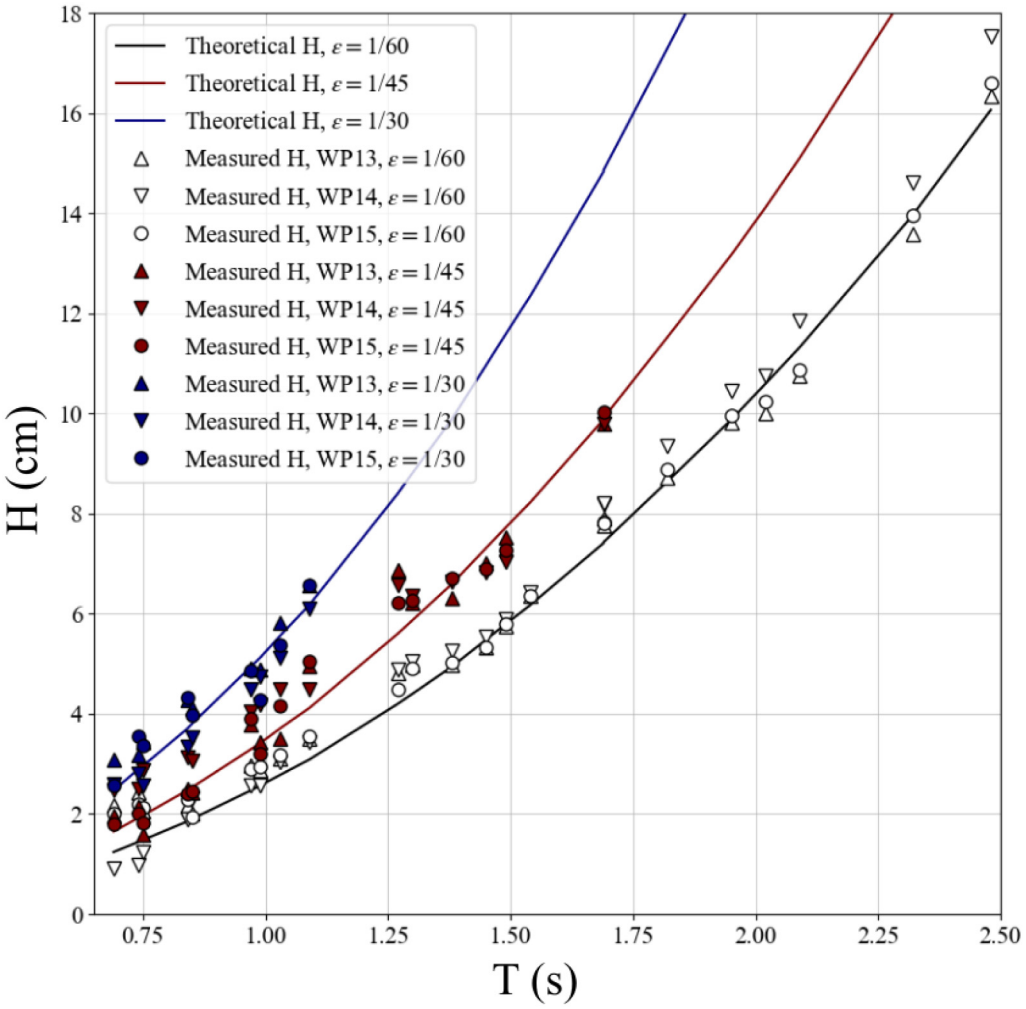

Fig. 2. Measured wave heights during incident wave documentation tests (without the cage model).

Surge $\eta_1(t)$ and sway $\eta_2(t)$ motions of the floater were calculated by averaging the positions of all eight Oqus balls along x and y axis, respectively. The first two vertical modes, $a_0(t)$ and $a_1(t)$, represent heave $\eta_3(t)$ and pitch $\eta_5(t)$ motions, respectively. The floater flexible modes are given by $a_n(t)$ (in the vertical plane) and $b_n(t)$ (in the horizontal plane), where $n \geq 2$. It is important to note that the radial mode, b_0(t), is removed from the Fourier series since it is not physical for the floater to expand radially.

2.1.3. Test conditions

Table 2 presents the test-matrix from the model tests. The performed tests are highlighted in grayscale and their wave heights in the model scale are given. The tests that could not be performed, mostly because of problems with waves overtopping due to the small freeboard, are blacked out. One of the tests with $T = 1.54$ s and $\varepsilon = 1/45$ had a problem with the video data and it could not be further analyzed. The wave steepness ε is calculated from the ratio between wave height and wavelength, i.e., $\varepsilon = H/\lambda$. The nondimensional wavelength (λ/D_{bag}) values are given and are used throughout the analysis, where the wavelength λ is calculated with linear wave dispersion relation. The full-scale value of each wave height would correlate to a classified wave level according to NS9415 (2009), and the level ranges from small to extreme. Note that the wave period T is not considered in classifying the waves, and the wave classification should thus only be taken as a crude indication of the severity of the considered regular waves.

Incident wave elevation ζ_a was documented before the model tests when the model was not present at the towing tank. The theoretical and measured steady-state wave heights are presented in Fig. 2. Three wave-probes measured the wave elevations in the vicinity of the model position (see Fig. 1), and these measurements were used to represent the undisturbed wave train for the analysis. The generated wave periods were found to be in good agreement with the desired periods as the averages from all probes lie around 99%–100% of their theoretical values. The measured wave heights

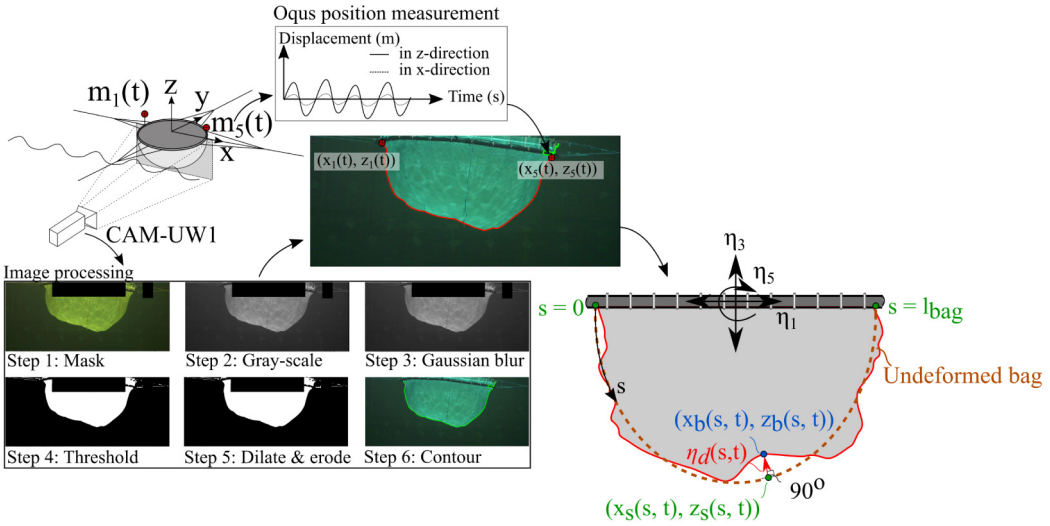

Fig. 3. Summary of the image processing. The bottom figures show the conversion of an original image to a binary image. Additional information regarding how Oqus positions were incorporated is also provided. The definition of bag motion is given in the bottom-right part of the figure.

deviated from their desired values, mainly for the short wave. The obtained steady-state heights of those cases showed differences between ±4%–75% of their theoretical values. However, this error was less significant for longer waves. The error (i.e., the difference between measured and theoretical wave height) was calculated for each wave probe. The wave probe with the smallest error, WP-13, was chosen for further analysis.

2.1.4. Free surge decay tests

Surge damping ratio ξ_1 (approximately 10%) and natural period $T_{N,1}$ (approximately 23.5 s) in model scale were estimated from free decay tests. The tests for other rigid body modes (i.e., heave and pitch) were not performed due to practical challenges related to perturbing the model in those modes. Tension on mooring lines, floater acceleration, and position were measured. Damping level and natural period were calculated using logarithmic decrement.

It is relevant to make some comments about surge response here. Due to the low damping rate and high surge natural period, steady-state surge response was not achieved in all of the experiment test conditions. This is because the transient part of the surge response did not fully disappear in each test. Based on a simple estimation using one degree-of-freedom forced motion equation, the decay time of the transient response in surge can be estimated by calculating the time at which the decay term in the homogeneous solution goes to zero (i.e., $e^{-\xi_1 \omega_{N,1} t} \rightarrow 0$, where $\omega_{N,1}$ is $2\pi/T_{N,1}$). The homogeneous term was found to be negligible after approximately t ≈ 200 s. The duration of each test was 180 s, including the time the wave needed to reach the model. Therefore, a longer test duration is required to negate the transient surge. The transient surge will act as a quasi-static current to the model, and it will influence the load and deformation on the bag.

2.2. Quantitative image analysis

Fig. 3 summarizes the method used to quantify bag motion. Recorded videos from the side-underwater camera (i.e., CAM-UW1 in Fig. 1) were used for the analysis. Since the camera could not perceive the object's depth, only the deformation in the x-z plane was treated (i.e., bag contour). The bag contour was defined as a line that separates the bag and surrounding water. The evolution of bag contour in time was analyzed in OpenCV (Bradski, 2000). The image processing technique was similar to Kristiansen et al. (2018c), where the goal was to extract coordinate information (in pixels) of the bag contour. This required binary images; hence, the original images were converted by employing mask, grayscale, blur, threshold, dilate, and erode. We also fed the information about floater position from Oqus balls OQ-1 and OQ-5 into the image analysis. This additional step was performed due to the difficulty in accurately capturing those two points by pure image manipulation, as the waves and the light conditions change over time. If some of the input parameters were unsuitable for manipulating the images as intended, unwanted details within the frame could be identified as part of the bag contour. An example is given in step 6 of Fig. 3, where the reflection on the water surface was identified as a part of the bag contour.

Further, quantitative information of bag contour position in an image was converted to a physical unit of length using transformation factor γ. The factor γ was found by relating the known bag diameter D_{bag} (in meters) and the pixel size of

bag diameter D_{img}, i.e. $\gamma = D_{bag} / D_{img}$. On the other hand, $1 / \gamma$ was utilized when we incorporated the measurements from OQ-1 and OQ-5 into the image analysis. Therefore, D_{img} can be found using:

$$D_{img} = | x_1(0) - x_5(0)| / \gamma \tag{3}$$

We assumed small camera distortion and that γ can be applied for all directions of the image coordinate system. We are fully aware of the importance of calibrating the camera before performing any image analysis, especially when one wants to extract information about the physical length from the images. However, the videos were initially not intended for this image analysis, and the camera CAM-UW1 was not calibrated. This represents a source of error in our data and analysis.

The transformed bag contour was further analyzed to obtain bag motion. The figure to the bottom-right of Fig. 3 illustrates the bag motion definition adapted for this study. The motion was imagined relative to an undeformed bag performing surge $\widetilde{\eta_1}$, heave $\widetilde{\eta_3}$, and pitch $\widetilde{\eta_5}$, respectively. The undeformed bag designation was defined by the bag static shape (i.e., bag shape in calm water conditions). A curvilinear axis s along the undeformed bag was taken as the reference line for bag motion measurement, where s = 0 and l_{bag} are points at the top-left and top-right of the undeformed bag, respectively. Measurements from Oqus balls OQ-1 (i.e., $[x_s(s = 0,\ t),\ z_s(s = 0,\ t)]$) and OQ-5 (i.e., $[x_s(s = l_{bag},\ t),\ z_s(s = l_{bag},\ t)]$) were utilized to obtain linear rigid body modes of the undeformed bag using:

$$\begin{aligned} \widetilde{\eta_1}(t) &= [x_s(s=0,\ t) + x_s(s=l_{bag},\ t)] / 2 \\ \widetilde{\eta_3}(t) &= [z_s(s=0,\ t) + z_s(s=l_{bag},\ t)] / 2 \\ \widetilde{\eta_5}(t) &= [z_s(s=0,\ t) - z_s(s=l_{bag},\ t)] / D_{bag} \\ [x_s(s,t), z_s(s,t)] &= [\widetilde{\eta_1} + z\widetilde{\eta_5}]\ \vec{\boldsymbol{i}} + [\widetilde{\eta_3} - x\ \widetilde{\eta_5}]\ \vec{\boldsymbol{k}} \end{aligned} \tag{4}$$

Hence, for a particular point along s, bag motion $\eta_d(s,\ t)$ was found by calculating the normal distance between points on the undeformed and deformed bag surface (i.e., $[x_b(s,\ t),\ z_b(s,\ t)]$). Here we define positive bag motion as a motion directed into internal water volume. Some interpolation process was involved in determining $x_b(s,\ t)$ and $z_b(s,\ t)$ since the points found by image analysis may not be normal to the points $[x_s(s,\ t),\ z_s(s,\ t)]$.

2.3. Signal processing

The measured time series from the sensors and bag motion were further analyzed. The steady-state time series of each test was determined based on the end of transient start-up and wave reflection from the parabolic beach. Wavefront propagation speed was calculated using group velocity of linear wave theory for deep water. The steady-state time series was then tapered at both ends using the Bingham window (Newland, 2011, p. 146), this was done to reduce end-effects and sharpen the spectrum during spectral analysis. The first harmonic component of the time series was extracted by multiplying the series' spectrum by a Gaussian mask in the frequency domain, retaining energy components within the frequency range of $\frac{0.9}{T} \leq f \leq \frac{1.1}{T}$. Transient surge response, which is discussed in Section 2.1.4, was then filtered out, and it was assumed that there would be no energy transfer between the wave frequency motions and the transient surge motion (i.e., both periods are well-separated). Finally, a Response Amplitude Operator (RAO) was calculated by taking the square root of the energy ratio between the first harmonic component of the response mode and the undisturbed incident wave elevation (i.e., RAO = $\eta_i / \zeta_a = \sqrt{E_{response} / E_{wave}}$).

3. Results and discussions

3.1. Static bag shapes in calm water

Bag shapes in calm water (i.e., before the wave forces act on the model) obtained from the image analysis are presented in Fig. 4. The shapes are represented by the mean value and the standard deviation of points along the bag contour. They are differentiated based on their test round, where for each test round, waves with constant steepness and increasing wave periods were run consecutively. This was committed to show that the bag static shape might change through the testing period.

Cage diameter in the x-z plane was found by calculating horizontal distance as measured by OQ-1 and OQ-5, where the mean diameter from all tests was 1.64 m (i.e., 9% larger than D_{bag}). In addition, measurements from the eight Oqus balls indicate that the floater assumed a somewhat oval shape. Therefore, as reference shapes for the discussion, two semicircles with diameter D_{bag} and 1.09 D_{bag} = 1.64 m are also presented. The static bag shapes are found somewhere between the two semicircles, except at the upper and lower parts. Their shapes are not semicircles; they are more like half-ovals. The static shape deviation from a semicircle might be due to three reasons: image capturing problem, manufacturing error, and a low bag filling level. Firstly, due to the finite distance between the bag model and the underwater camera, our video recording might capture a smaller bag contour that is closer to the camera (i.e., the x-z plane of the bag at y < 0 in Fig. 1). Secondly, due to the nature of fabric, which adjusts its shape under static and dynamic loads, it was difficult to achieve high precision in the manufacturing process. Hence, sewing a perfect half-sphere shape out of eight fabric sheets was difficult to achieve. Thirdly, bag shape in equilibrium is strongly dependent on several parameters, for instance: filling

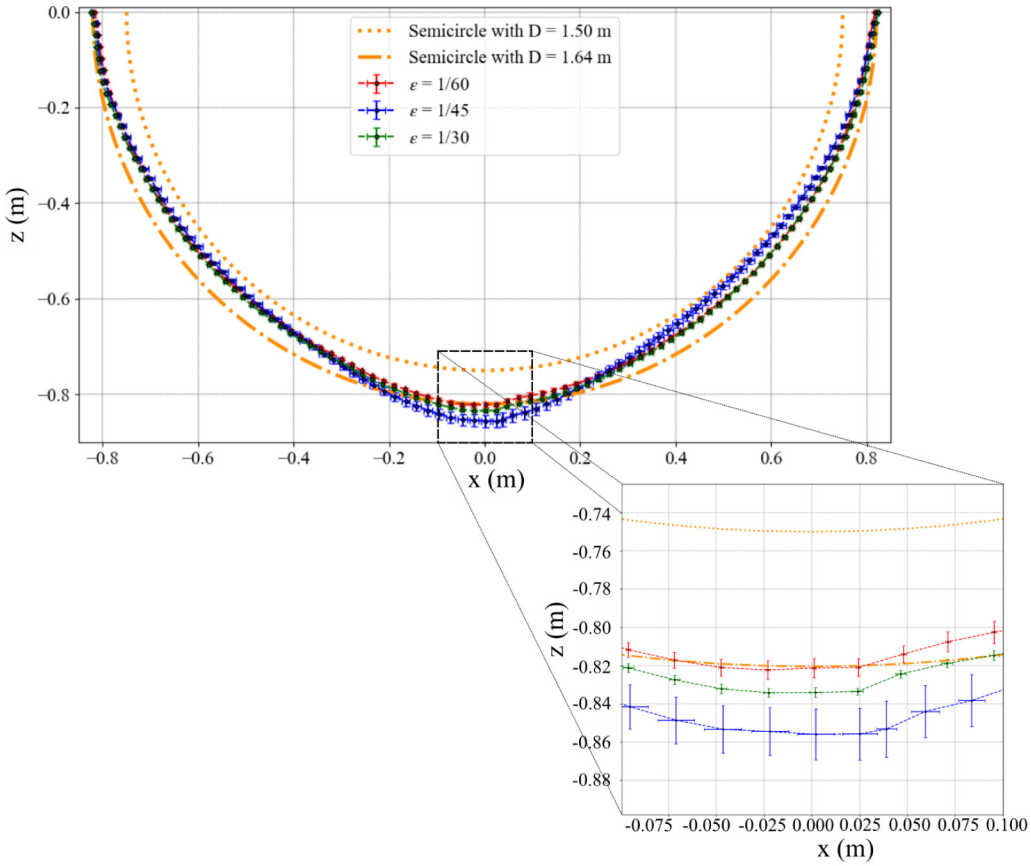

Fig. 4. Static bag shapes (i.e., in calm water conditions) in different test rounds. The shapes are represented by the mean value and the standard deviation of points along the bag contour. They are differentiated based on their test round, where for each test round, waves with constant steepness and increasing wave periods were run consecutively.

level and the resulting fabric pretension, fabric elasticity, and load history (Løland and Aarsnes, 1994; Strand et al., 2014). Assuming that the fabric elasticity was unchanged over the testing period, we believe that the bag filling level had the most significant influence on defining the static bag shapes.

It is also interesting to compare the mean value of the test $\varepsilon = 1/45$ with the other test rounds, where it shows a larger draught and some contraction on the aft-side. In addition, the standard deviation, especially around the lower part, is more significant. These results may indicate that the bag was not sufficiently filled during the test round $\varepsilon = 1/45$, which may be due to a lower filling level than 100.1%. Change of filling level during the tests could be due to waterproofness of the bag, wave overtopping, and spilling. The bag was sewn with thread, which made it not entirely watertight, and a small amount of water might go in and out of the bag through the sewn parts. With sufficiently steep wave height, the waves might overtop the cage freeboard. On the other hand, the water might spill out of the bag under sufficiently large sloshing amplitude. However, we only monitored the water volumes visually by observing the floater submergence, and we have no quantitative data on the water level changes inside the bag. Lader et al. (2017) discussed the consequence of having 70% filling level inside the bag, and they concluded that the floater responses were somewhat decoupled from bag motion and better followed the incident waves than the fully filled one. Hence, this may represent one error source for the test results of $\varepsilon = 1/45$.

The presented results emphasize a need to monitor and maintain the bag's internal water volume during the model tests, when the internal water volume has a significant effect on the cages' responses. It is desirable to have a similar bag condition throughout the tests so that errors that arise from differences in bag shapes and internal water volume can be avoided. A possible procedure could be to have a cage model with a higher overfilling level than that in the present model, which requires a floater with a larger cross-section diameter. The intended cage draught due to overfilling could be more accurately quantified (e.g., with Oqus balls) and kept constant throughout the tests.

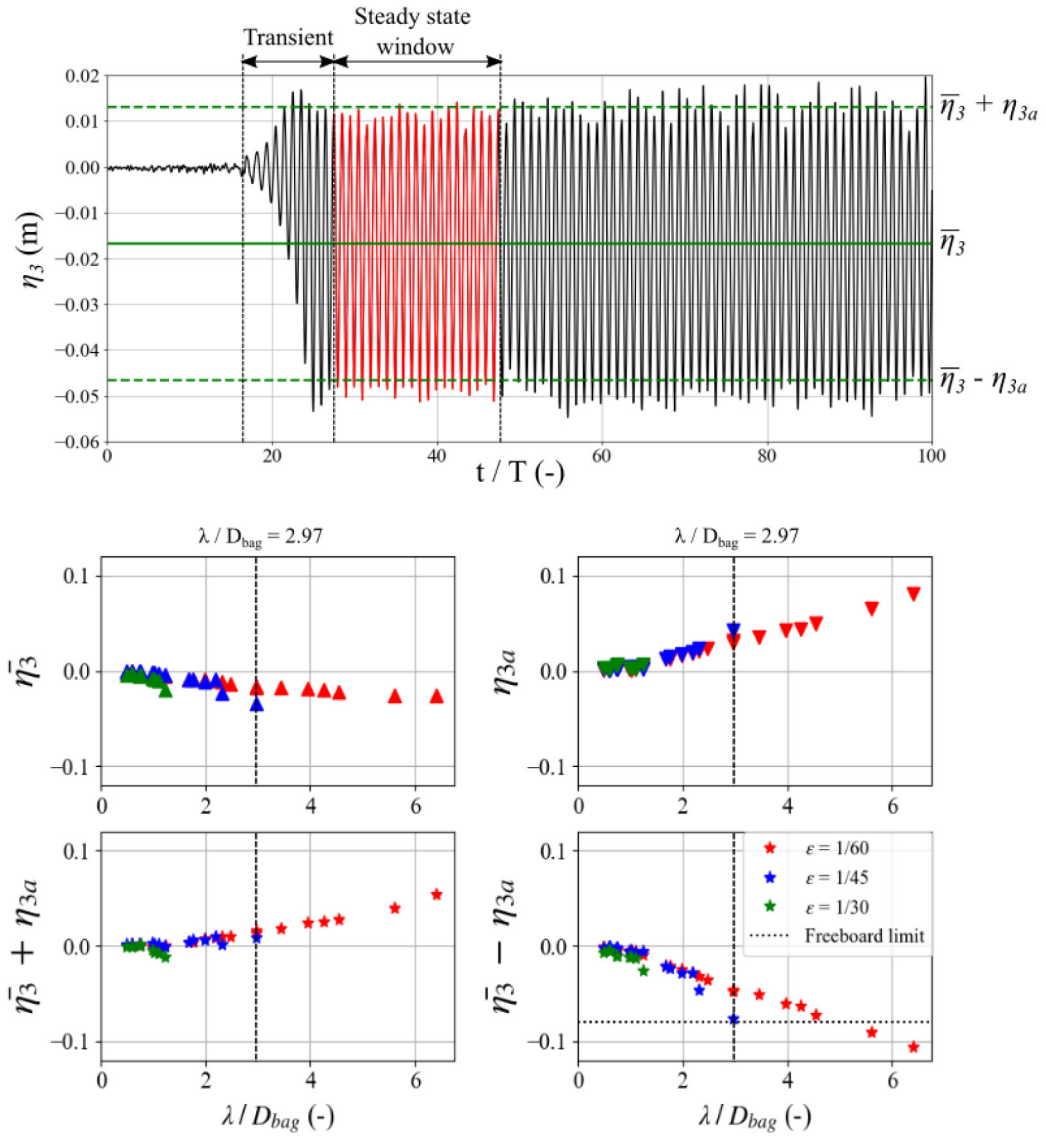

Fig. 5. Time series of floater motion in heave for $\lambda/D_{bag} = 2.97$ and $\varepsilon = 1/60$ is given in the upper portion. The bottom portion gives cage set-down analysis results as a function of wave steepnesses ε and nondimensional wavelength λ/D_{bag}.

3.2. Cage set-down

It was visually observed and measured that the cage model oscillated vertically with a non-zero mean value under wave forces, i.e., the cage was set-down and occupied a different mean vertical position than that in calm water conditions. The set-down magnitude was observed to increase under longer and steeper waves. An example of the heave time series from the test with $\lambda/D_{bag} = 2.97$ and $\varepsilon = 1/60$ is given in the top part of Fig. 5. We calculated the cage set-down by two means: Oqus sensors and image analysis (this calculation is explained in Fig. 3, but without use of the Oqus sensor). Thus, both measurements were independent of each other. We quantified the set-down by calculating the heave mean value $\bar{\eta}_3$ and heave amplitude $\eta_{3a} = \sqrt{2}\sigma_{\eta_3}$ of the steady-state heave time series, where σ_{η_3} is the standard deviation of heave response.

The bottom part of Fig. 5 shows increasingly negative mean heave values with increasing incident wavelength and wave steepness. On the other hand, the figure also shows an increase in heave amplitudes. The combination of both effects has two consequences: decreased internal water volume integrity and a decrease in cage pretension. The former indicates a water exchange between the internal volume of the cage and the surrounding water, which was one of the reasons for some of the halted tests indicated in Table 2. We wanted to maintain the cage model's internal water mass as

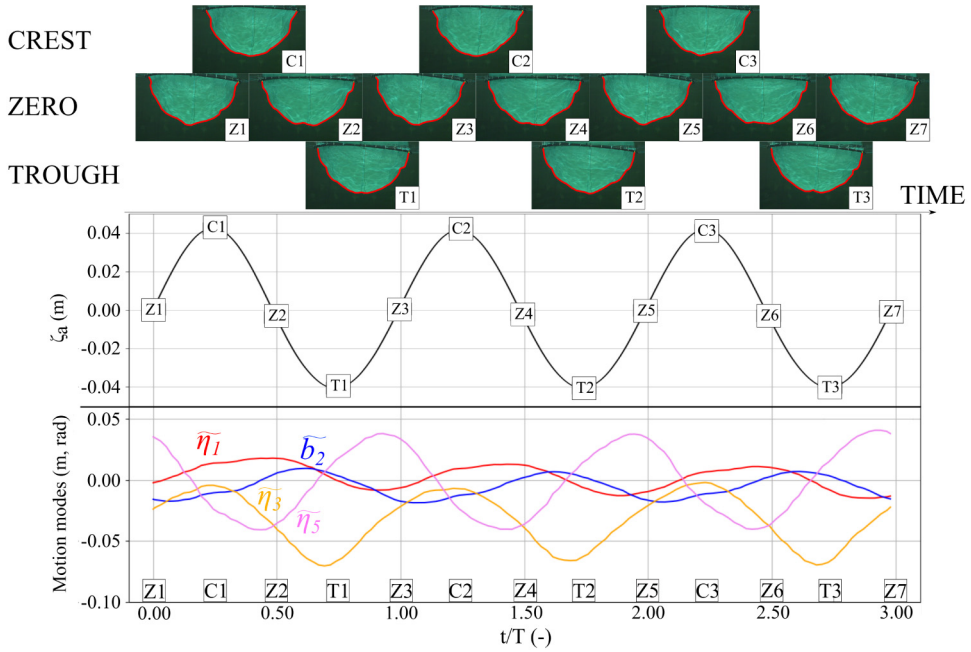

Fig. 6. From top to bottom: captured frames from the recorded videos, time series of measured wave elevation, and time series of motion modes of the floater. The labels on the captured frames indicate where they occurred in the other two portions of the figure. WP14 was used for visualization purposes because it was located near the transverse-center line of the bag (see Fig. 1). The abscissa t/T is a dimensionless time normalized by the wave period. The selected window was chosen to coincide with steady measurement of the incident waves by WP14, and t/T begins at zero only for illustration purposes. See Video 1 for the full video.

similar as possible in all the tests; hence, the tests were stopped when there was indication of significant water exchange over the model's rim. The analysis results in the bottom-right of Fig. 5 show that some of the heave motions exceeded the model's freeboard. The second consequence, decreased bag pretension, is caused by an increase in external hydrostatic pressure at the new mean position.

The cage set-down must be studied theoretically to identify the main contributing factors that caused this effect. Possible candidates are mean heave force due to the exterior flow problem, and coupling with the bag flexible modes. The latter is due to the membrane's inability to take compressive force from hydrodynamic pressure at the bag bottom. Hence, throughout a load cycle, the bag contributes only by imposing downward forces on the floater. This might explain the increasing trends of the set-down for longer and steeper incident waves. In order to perform a hydrodynamic analysis of a fabric membrane cage, the cage static configuration is needed (see, e.g., Strand and Faltinsen (2019)). If the set-down effect is not accounted for in the analysis, which the effect may change the cage static configuration, the prediction of loads on and responses of the cage might be less accurate.

3.3. Wavelike bag motion

The observed wavelike bag motion (or bag wave) is presented in this section. The bag wave can be described as a nearly periodic propagating fabric motion originating from the bag's attachment to the floater. This motion travels down to the bag bottom over a period that is approximately equal to the incident wave period. The bag motion in our analysis $\eta_d(s,t)$ is defined in Fig. 3. Observation from one of the tests is discussed in Section 3.3.1. The first harmonic analysis of the bag wave is presented and discussed in Section 3.3.2.

3.3.1. Observation

Video snap-shots and floater response measurements, taken from the test with $\lambda\ /\ D_{bag} = 2.97$ and steepness $\varepsilon = 1/60$, are presented in Fig. 6. The associated video is given in the Supplementary materials (see Video 1). This particular case has been chosen due to significant bag bottom motion, as shown in Section 3.3.2. However, the observed phenomenon is similar to the other tested incident wave periods and steepnesses, except for a couple of shorter wave periods where the bag motion did not propagate downward. For the purpose of illustration, the presented results cover three incident wave periods. In addition, to describe the floater motion in the x-z plane, motions from OQ-1 and OQ-5 were calculated through use of Eq. (4). In this plane, ovalization mode can be obtained using:

$$\widetilde{b_2}(t) \;=\; [x_s(s = l_{bag},\ t) \;-\; x_s(s = 0,\ t) \;-\; D_{bag}]\ /\ 2 \tag{5}$$

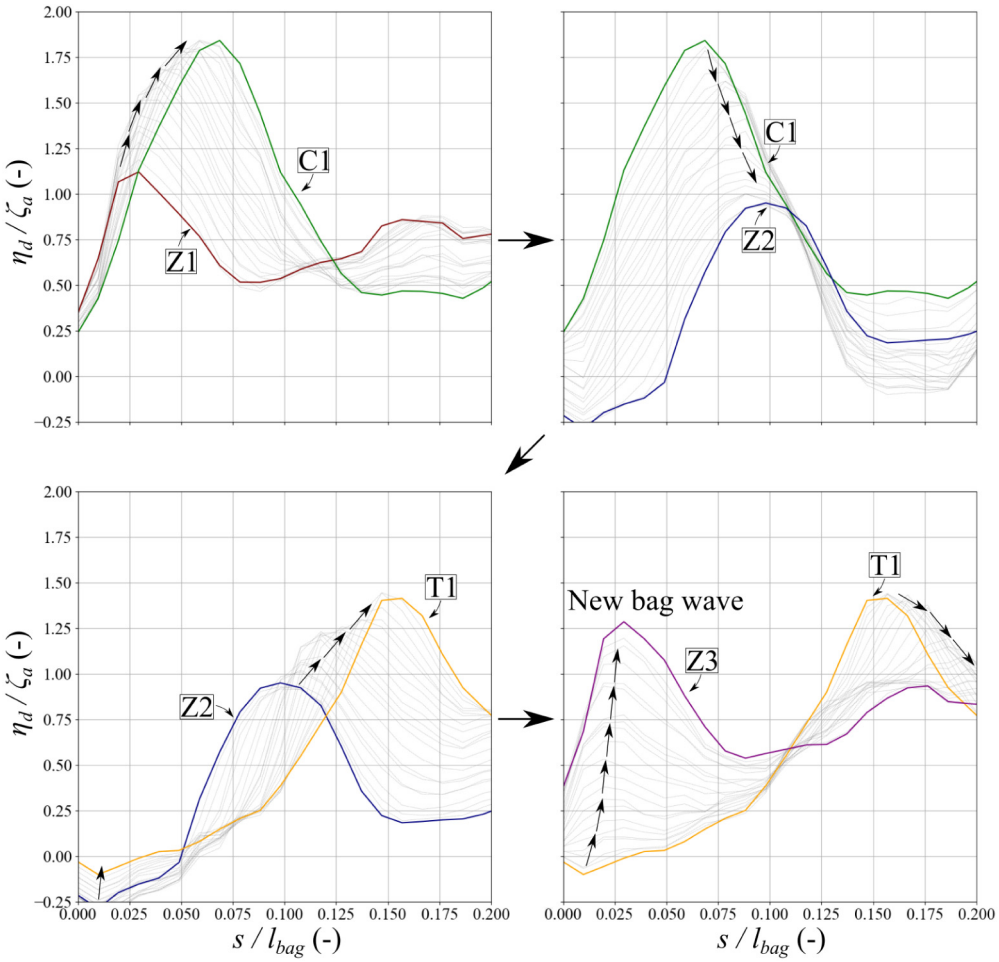

Fig. 7. Illustration of the bag wave by the non-dimensionalized bag motion amplitude η_d/ζ_a. The time instances are as indicated in Fig. 6. Arrows are used to clarify the time evolution of the bag wave.

The bag wave can be described by $Zm \rightarrow Cm \rightarrow Z2m \rightarrow Tm \rightarrow Z(2m+1)$ in Fig. 6, where m = 1, 2, and 3. The bag wave was initiated when the model was at the wave crest (see time instance C1, for example), at which point the bag deformed nearly symmetrically around the plane x = 0 and formed a contraction at the fore and aft sides of the floater. Thereafter, the bag wave traveled down to the bag bottom as the cage followed down the wave trough (see, e.g., Z2 and T1, respectively). The quantitative description of the bag wave is illustrated in Fig. 7, where, for clarity, only the non-dimensionalized bag motion amplitude η_d/ζ_a along $0 < s/l_{bag} < 0.2$ is presented. It is apparent that the bag wave was initiated on the bag part near the floater, and it propagated with varying bag motion amplitude. It can also be observed that a new bag wave was generated at the end of one period of oscillation.

One possible consequence of the bag wave is significant influence on the bag bottom dynamics. The test presented in Fig. 6 found that vertical acceleration measurement at the bag bottom was more significant than that at the floater, and these results are depicted in Fig. 8. The nature of the acceleration time series indicates the presence of snap loads, which can be an issue for the strength and fatigue of the fabric material. We attempted to compare the acceleration measurement at the bag bottom with our image analysis results, but we did not find significant correlations between them. Our image analysis may not have captured the actual motion of the center point of the bag bottom, as it was outside the camera view for a significant portion of the load cycles. Further, large-amplitude high frequency accelerations do not necessarily lead to large amplitude motions.

It is also interesting to note how the bag deformation changes from one wave cycle to another wave cycle. Fig. 9 illustrates how the bag motion amplitude η_d varies at time instances Z1, Z3, Z5, and Z7. This might be due to quasi-static "current" from transient surge motion (see Section 2.1.4). The transient surge motion induces external quasi-static pressure, which may affect the bag deformation and tension. In addition, Fig. 9 shows a more significant difference on the bottom part of the bag, which signifies a more complex dynamic at the bottom of the bag (i.e., significant energy

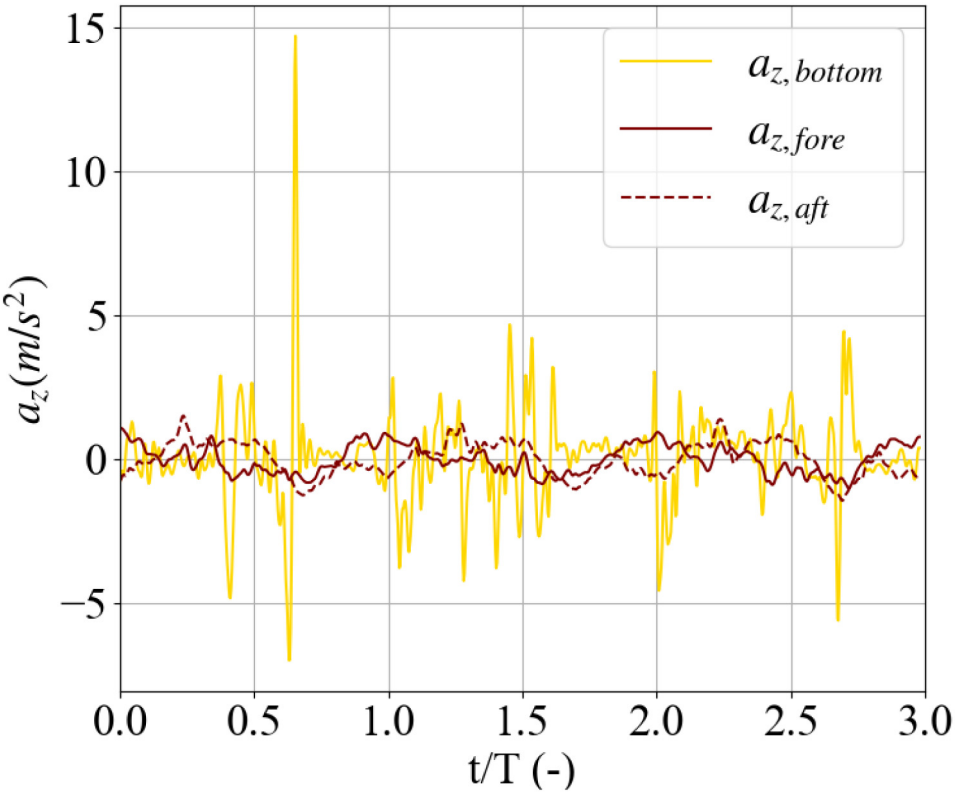

Fig. 8. Comparison of the measured vertical acceleration a_z at the floater and at the bag bottom. The time window is similar to that of Fig. 6.

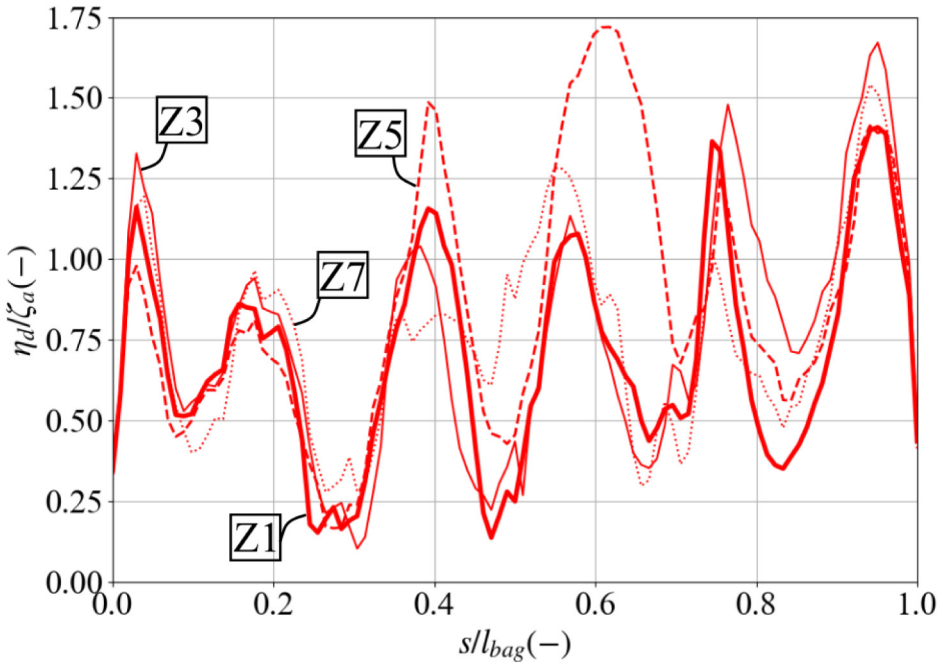

Fig. 9. Results of the non-dimensionalized bag motion amplitude η_d/ζ_a along the bag contour s/l_{bag} at time instances Z1, Z3, Z5, and Z7. The time instances are as indicated in Fig. 6.

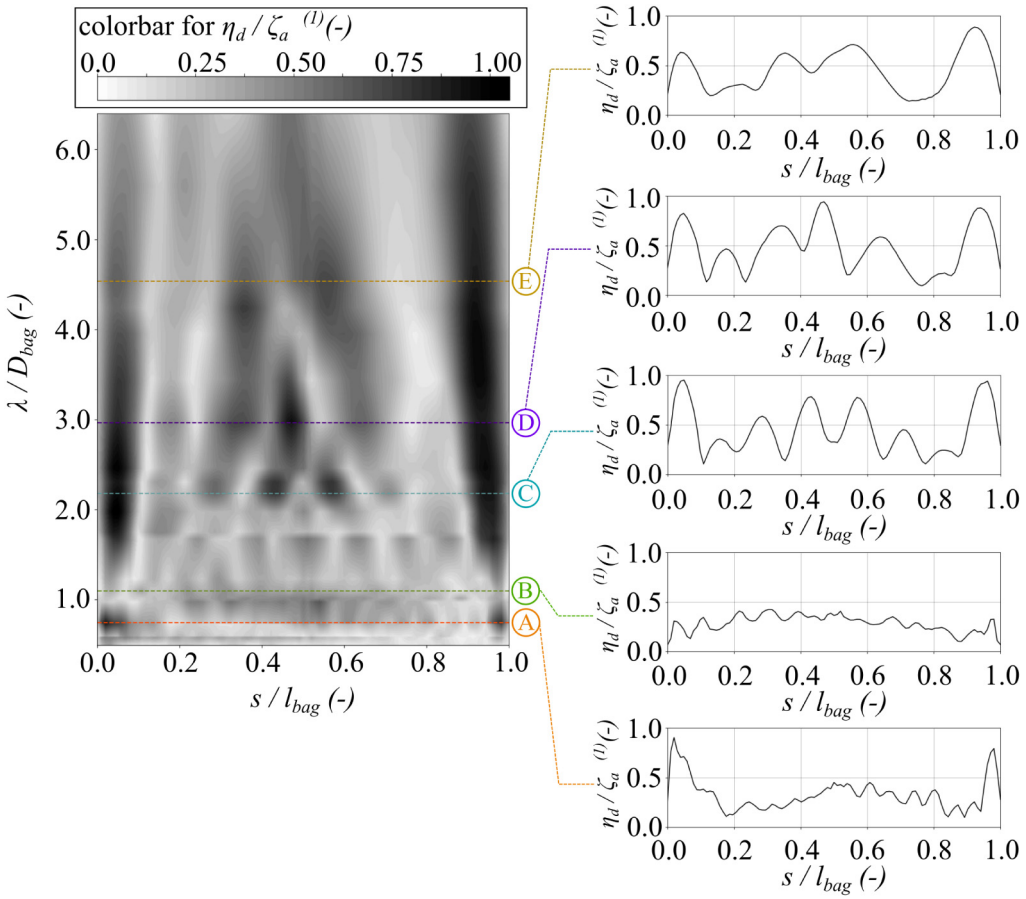

Fig. 10. Figure on the left is a contour plot of $\eta_d/\zeta_a^{(1)}$ results from the tests with wave steepness $\varepsilon = 1/60$. The scale of $\eta_d/\zeta_a^{(1)}$ is given as a grayscale bar indicated within the figure, where the range goes from low (white) to high (black). Comparison of $\eta_d/\zeta_a^{(1)}$ for $\lambda/D_{bag} = 0.76$, 1.12, 2.19, 2.9, and 4.53, is given in the right portion of the figure.

from other harmonic components). Another reason may be snap loads which introduce nonlinear responses, such that a periodic solution is not necessarily the only solution.

3.3.2. First harmonic bag motion

The first harmonic component of non-dimensionalized bag motion amplitude $\eta_d/\zeta_a{}^{(1)}$ is analyzed in this section. The results for tests with incident wave steepness $\varepsilon = 1/60$ are shown in Fig. 10. The abscissa and ordinate of the figure define the point location s on the bag contour, and motion amplitude of that point at the tested wave period, respectively. In general, the amplitude of bag motion differs at different locations along the bag and for different incident wave periods and steepnesses.

Fig. 10 shows that, in most of the tested incident wave periods, $\eta_d/\zeta_a{}^{(1)}$ have localized peaks near $s = 0$ and l_{bag} (i.e., near the floater). Hydrodynamic pressures from incident waves and sloshing have the highest magnitude near the free surface zone; hence, the part of the bag near that zone tends to deform more than the other parts. It can also be observed that the peaks become somewhat wider with increasing incident wavelength. However, the results show that with a sufficiently long wavelength the peaks of the aft-part are higher than those of the fore-part. People have reported in tests with floater only that the aft part of the floater moves more in the horizontal plane than the fore part (Li, P., personal communication, 2020). In addition, near-cancellation of bag motion amplitude near the floater can be observed around the first symmetric sloshing mode of the rigid half-sphere tank at $T_{2,1} = 1.04$ s (see, e.g., Mciver (1989)) or at $\lambda/D_{bag} = 1.12$, which may indicate forces in approximately opposite phases (the incident wave and sloshing) acting on both sides of the surface of the bag.

The right portion of Fig. 10 shows that the bag motions at $s = l_{bag}/2$ (i.e., at bag bottom) tend to increase with a longer incident wavelength. Prominent peaks of $\eta_d/\zeta_a{}^{(1)}$ can be observed for the test conditions $\lambda/D_{bag} = 2.19$ and 2.97, which exemplifies the consequence of the observed bag wave. As discussed in Section 3.3.1, the bag wave amplifies the motion of the bag bottom.

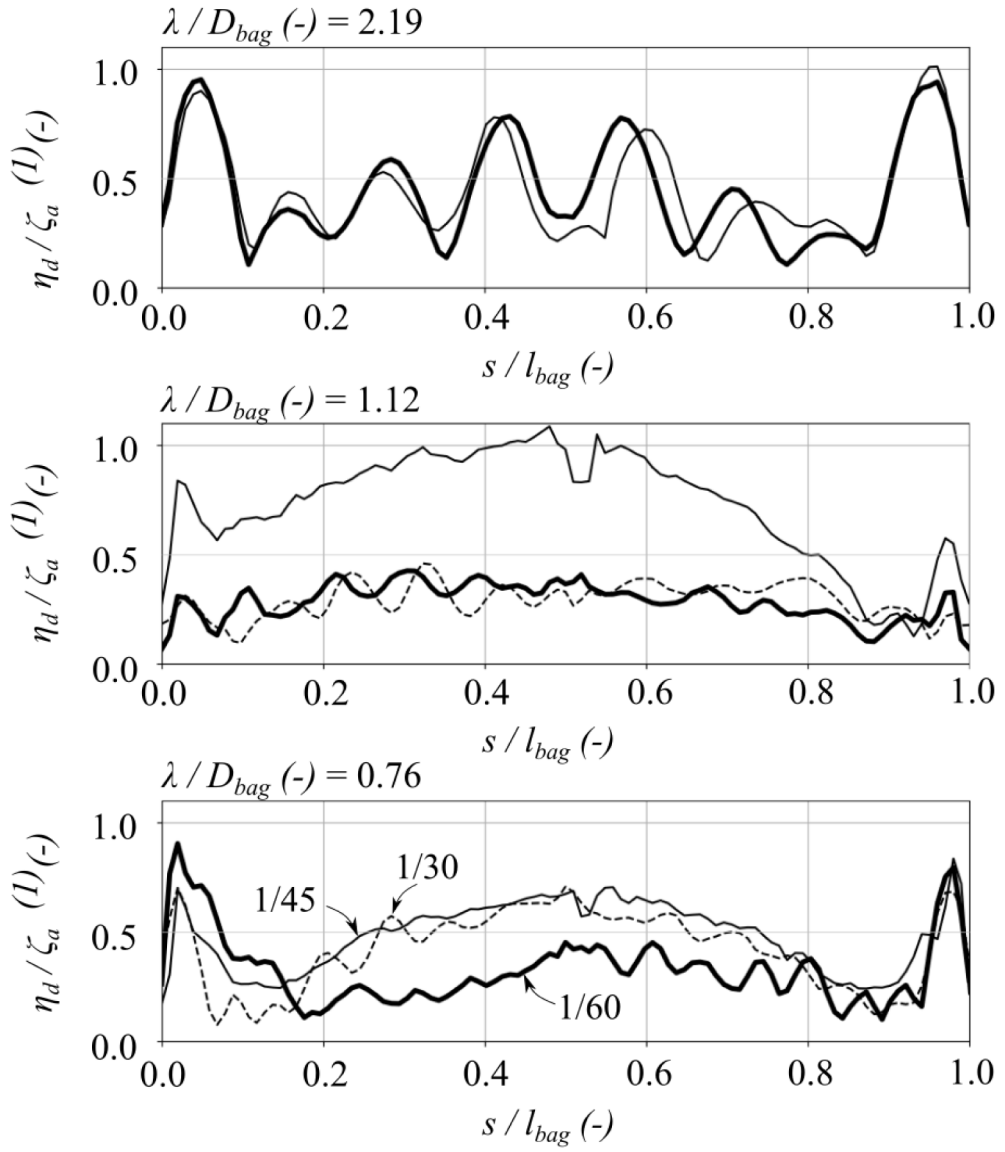

Fig. 11. Effect of wave steepness on the bag normal motion $\eta_d/\zeta_a{}^{(1)}$ for test cases $\lambda/D_{bag} = 0.76$, 1.11, and 2.19. The different line styles represent cases with different wave steepness, as indicated in the bottom part of the figure. Note that the sudden drop of $\eta_d/\zeta_a{}^{(1)}$ around $s/l_{bag} = 0.5$ for the test with $\varepsilon = 1/45$ is due to the error in image analysis explained in Section 2.2.

Lastly, the effect of wave steepness on the bag motion is illustrated in Fig. 11. The presented cases are the tests with $\lambda/D_{bag} = 0.76$, 1.12, and 2.19 in Fig. 10. The bag motion amplitudes show a highly nonlinear characteristic: they are either amplified by or comparable with increasing wave steepness, and their differences vary along the bag contour. Significant amplification can be observed for the test with $\varepsilon = 1/45$ and $\lambda/D_{bag} = 1.12$, while the test with $\varepsilon = 1/30$ does not show such behavior (see the middle part of Fig. 11). One plausible explanation is the lower bag pretension discussed in Section 3.1. Hence, less bag stiffness for the test with $\varepsilon = 1/45$ resulted in significantly higher bag motion amplitudes.

3.4. First harmonic floater motions

Comparison of the experimental and numerical results of floater RAOs in the surge, heave, and pitch modes are presented and discussed in Section 3.4.2. The experimental RAOs are compared against numerical results from WAMIT and the numerical model is briefly discussed in Section 3.4.1. A rigid cage was utilized in the numerical model in order to identify and discuss the limitations of rigid body assumptions in the analysis of floater motions for the fabric membrane cage. Note that the RAOs from the experiment are based on the first harmonic component of steady-state responses as

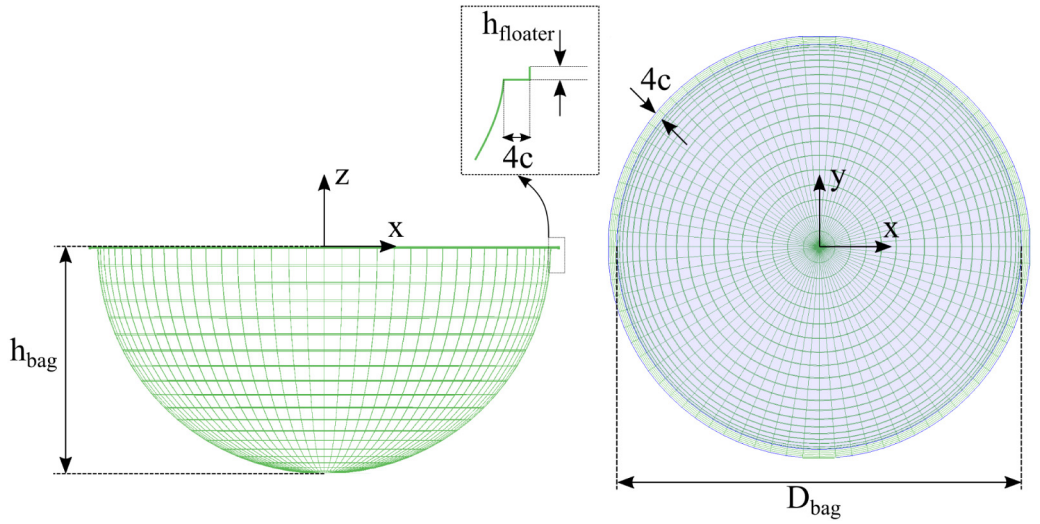

Fig. 12. Illustration of cage model discretization using low-order panel method in which only the mean wetted surfaces of the cage are discretized. The meshes for the internal tank are represented by the blue part of the model, but because the fabric was assumed to be very thin, the distinction between internal and external surface meshes is not apparent. The floater model was simplified as described in the paragraph above, yielding $h_{floater}$ = 6.28 mm. (For interpretation of the references to color in this figure legend, the reader is referred to the web version of this article.)

discussed in Section 2.3. The method used to obtain the rigid body modes and the floater's vertical flexible modes from the floater's position measurements is explained in Section 2.1.2.

3.4.1. Brief description of numerical modeling in WAMIT

WAMIT solves linear wave–structure interaction problems in the frequency domain. In this study, the moored cage was assumed to float in a water domain with infinite depth. Model arrangement and wave propagation direction similar to that in the experiment was implemented in the WAMIT model. However, the bag was modeled as a rigid wall with geometrical dimensions and thickness similar to that of the model tests. Therefore, the floater and bag flexible modes were not modeled. The floater geometry was simplified to avoid numerical problems, but we retained water-plane area and displacement values similar to those of a half-submerged double tori floater. The low-order panel method was used to discretize the numerical cage model, which means that the velocity potential was approximated by piecewise constant on each quadrilateral panel. WAMIT's internal tank utility was utilized to model the internal water mass, which required the numerical cage model to be discretized on its inner and outer surfaces. Illustration of the discretized cage model with coarse mesh is depicted in Fig. 12. By taking advantage of the cage's two planes of symmetry (i.e., x-z and y-z planes), 8400 quadrilateral panels were used to represent one-quarter of the cage. The mooring lines were modeled as linear spring forces with corresponding coefficients:

$$\begin{aligned} C_{11,moor} &= 2\,k_s\,\cos\,\alpha \\ C_{33,moor} &= 2\,k_s\,\sin\,\alpha \\ C_{55,moor} &= D_{bag}\,T_{0,m} \end{aligned} \tag{6}$$

The value of each of these parameters is given in Section 2.1.1.

3.4.2. Comparison between experimental and numerical results

The calculated coupled response RAOs are presented in Fig. 13. Experimental RAOs on different wave periods and steepnesses are given by various colored markers. Some test conditions were only repeated once, where the results are plotted by using identical markers with a gray color fill. It is not possible to draw a quantitative conclusion on the precision errors of our model test results, and more repetition tests should have been done. For the repeated tests, differences between results can only give qualitative indicators of the uncertainty in those results. The presented WAMIT RAOs consider the hydrodynamic coupling effects between sloshing, surge, and pitch modes for the studied rigid axisymmetric cage. In heave mode, the linear heave motion is decoupled from the other modes, and the internal water mass behaves as a frozen mass.

Before discussing the results, distinction between the three kinds of natural periods indicated in Fig. 13 should be clarified. All the natural periods are determined based on the rigid half-sphere cage, i.e., coupling effects with the bag and floater flexible modes were not considered during determination. The natural periods are presented as non-dimensionalized wavelength forms $\tilde{\lambda} = \lambda/D_{bag}$ that are consistent with the figure's axis. Firstly, the two highest

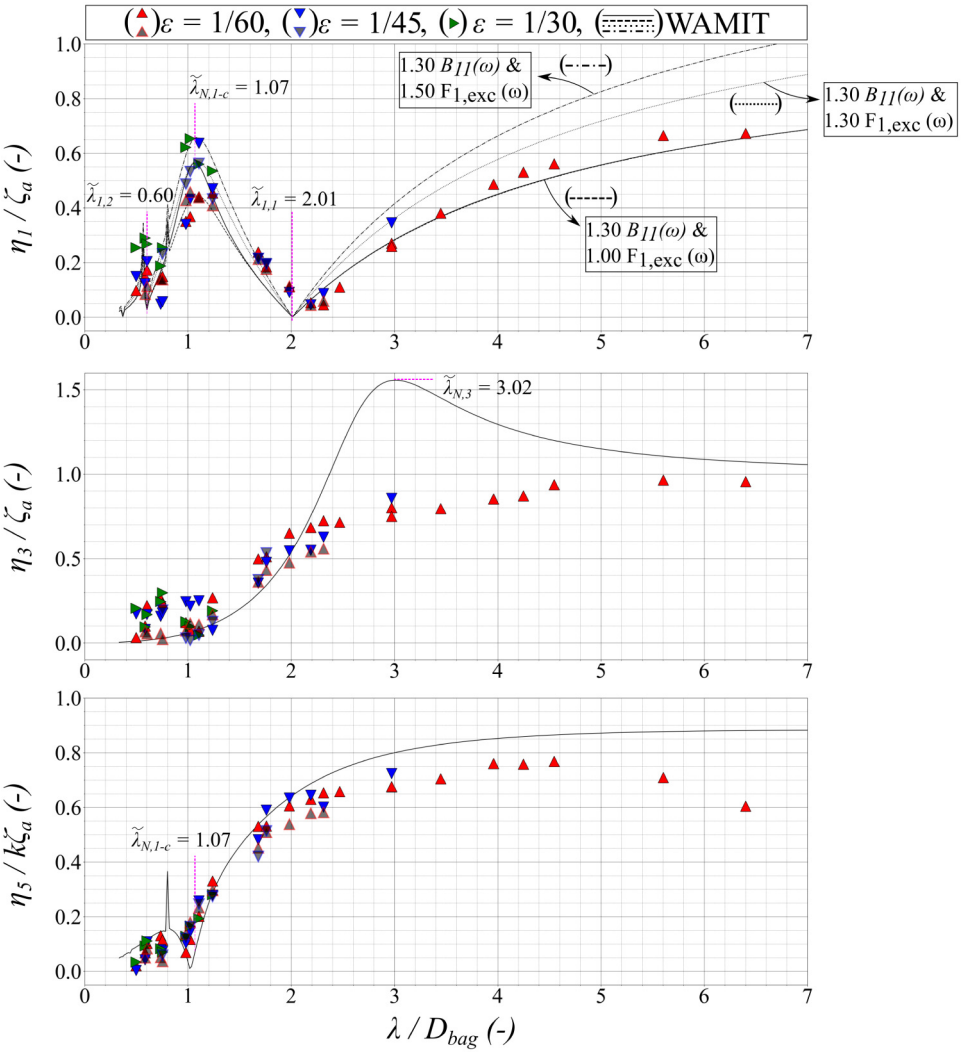

Fig. 13. Comparison of experiment (flexible) and WAMIT (rigid) coupled motion RAOs results. From top to bottom are RAO for surge, heave, and pitch motions. Natural periods of the rigid cage are indicated within the figure and are presented in non-dimensionalized wavelength forms $\tilde{\lambda} = \lambda / D_{bag}$. Parameters sensitivity of the WAMIT surge RAO to variation of the damping B_{11} and exciting force $F_{1,exc}$ in surge is presented, where the information about the artificially modified parameters is given in the surge RAO plot. (For interpretation of the references to color in this figure legend, the reader is referred to the web version of this article.)

eigenperiods of antisymmetric sloshing modes are denoted as $\tilde{\lambda}_{1,i}$, where $i = 1$ and 2. Extensive numerical results on the eigenperiods of the spherical tank were reported in Mciver (1989). The reported values of $\tilde{\lambda}_{1,1}$ and $\tilde{\lambda}_{1,2}$ are consistent with internal added-mass results $A_{11}^{(I)}$ from WAMIT where the added-mass at those periods is singular. Note that in a rigid spherical tank, the internal pressure does not cause any pitch moment, resulting in zero internal added mass in pitch (i.e., $A_{55}^{(I)} = A_{15}^{(I)} = A_{51}^{(I)} = 0$). Secondly, the coupled surge resonance period $\tilde{\lambda}_{N,1-c}$ can be, as a first estimation, calculated by solving undamped coupled surge-pitch equations of motion with no excitation force:

$$\left\{ -\omega^2 \begin{bmatrix} M + A_{11}(\omega) & I_{15} + A_{15}(\omega) \\ I_{51} + A_{51}(\omega) & I_{55} + A_{55}(\omega) \end{bmatrix} + \begin{bmatrix} C_{11} & C_{15} \\ C_{51} & C_{55} \end{bmatrix} \right\} \begin{bmatrix} \eta_1 \\ \eta_5 \end{bmatrix} = \begin{bmatrix} 0 \\ 0 \end{bmatrix} \tag{7}$$

Thirdly, the heave resonance period $\tilde{\lambda}_{N,3}$ can be found through use of the undamped heave equation of motion with no excitation force:

$$\left\{ -\omega^2 (M + A_{33}) + C_{33} \right\} \eta_3 = 0 \tag{8}$$

where M, I_{jk}, A_{jk}, and C_{jk} in Eqs. (7) and (8) are the cage dry mass, cage moment of inertia, added mass coefficient, and restoring coefficient, respectively. Note that the restoring contribution from the mooring lines (i.e., Eq. (6)) has to be

added to the hydrostatic restoring to determine the C_{jk} value. The frequency-dependent added-mass $A_{jk}(\omega)$ is the sum of the added-mass from the internal and external fluid flow (i.e., $A_{jk}(\omega) = A_{jk}^{(I)}(\omega) + A_{jk}^{(E)}(\omega)$).

Experimental heave RAO shows a deviation from the WAMIT prediction at the rigid cage's natural period in heave $\tilde{\lambda}_{N,3}$. As shown in Fig. 10, significant amplification of bag motion amplitude at bag bottom can be observed at that wave period. This shows a significant coupling effect between heave and the bag flexible modes rather than viscous damping, which possibly indicates that an additional wave radiation damping is being introduced to the heaving flexible bag. Therefore, the heave resonance peak is reduced, as shown by the experimental results. In addition, a small peak can be observed in the experimental heave RAO results at the vicinity of $0.5 \lesssim \lambda/D_{bag} \lesssim 1.2$. The peak occurs for every incident wave steepness with roughly similar magnitudes. However, the repetition tests do not show such peak, where they are approximately in the same range as WAMIT result. The reason of the inconsistent experimental results is not fully understood, but it might be attributed to the experimental uncertainties and the sensitiveness of the bag responses to the filling level.

Cancellations in WAMIT surge RAO can be observed at $\tilde{\lambda}_{1,1}$ and $\tilde{\lambda}_{1,2}$, the two lowest natural periods of antisymmetric sloshing modes in the half-sphere tank. WAMIT predicts infinite internal surge added mass at those wave periods, explaining this total cancellation behavior in the surge mode. Coupling with pitch mode does not markedly change the cancellation periods because pitch does not excite sloshing in a rigid half-sphere tank. However, the experiment shows a different cancellation period than $\tilde{\lambda}_{1,1}$, where the period is found to be approximately 10% higher. The bag flexible modes may contribute to the change of sloshing eigenperiods, as was shown by Strand and Faltinsen (2017) in their study of a two-dimensional rectangular tank with a flexible sidewall. The other possibility is that the nonlinear sloshing might matter for sufficiently large sloshing amplitude, where the assumption of constant sloshing eigenperiods might not be valid (Rognebakke and Faltinsen, 2003). In addition, the experimental results show non-zero but small surge responses at these cancellation periods. This can be attributed to the transfer of energy to higher sloshing modes, to viscous energy dissipation inside the cage, and possibly to damping attributed to bag deformations and interaction with the external fluid, which causes wave radiation.

Both flexible (experiment) and rigid (WAMIT) cages show significant effects of coupling between sloshing, surge, and pitch motions. A surge resonance peak can be observed at $\tilde{\lambda}_{N,1-c}$, while the pitch shows a nearly zero response amplitude. This shows a significant sloshing effect on the surge motion at that wave period, while the pitch motion is indirectly affected through the coupling with the surge motion and the exterior flow. The experimental surge RAOs also show resonance peaks around $\tilde{\lambda}_{N,1-c}$ but with a non-negligible dependency on incident wave steepness. Coincidentally, $\tilde{\lambda}_{N,1-c}$ is very close to the first symmetric sloshing natural period of the rigid half-sphere tank at $\tilde{\lambda}_{2,1} = 1.12$ (see e.g., Mciver (1989)). The nonlinear behavior at the coupled surge resonance period was also observed by Kristiansen et al. (2018b) in their study on a floating rigid cylindrical closed cage. They observed the presence of wave steepness-dependent antisymmetric sloshing at the first symmetric sloshing natural period of their cage model, where the period also coincided with their coupled surge resonance period. They suspected that the nonlinear effects of sloshing were causing this behavior. We attempted to investigate the contributing parameters for the observed surge nonlinearity by artificially changing selected parameters in WAMIT outputs. As presented in the upper portion of Fig. 13, we show how a 30%–50% higher excitation force $F_{1,exc}$ and 30% higher damping B_{11} might explain the amplitude-dependent surge response of the model test results. The question is why there is a higher surge excitation.

Based on the video recordings (see Video 2) and their snapshots (only the fore part) presented in Fig. 14, one can clearly observe that the fore and aft part of the floater goes in and out of water. The consequence is vertical viscous drag loads. The first six vertical flexible modes RAOs of the floater are presented in Fig. 15. The results show significant vertical flexible responses of the floater in the vicinity of the coupled surge natural period $\tilde{\lambda}_{N,1-c}$, and a large scatter of results is apparent. Due to the vertical relative motion between the floater and the free surface, drag forces might matter when a significant flow separation occurs. Depending on the phasing with the cage's surge motion, the drag forces experienced by the floater will give either additional damping or excitation surge force to the bag. We estimated the two-dimensional drag force using hydrodynamic screen model presented in Kristiansen and Faltinsen (2012), where the problem definition is illustrated in Fig. 14. For this purpose, the vertical relative displacement A_{rel} between the floater and the free surface at the fore part was crudely estimated from Video 2. The calculated drag force was then compared to the vertical Froude–Krylov force on a semi-submerged flexible torus, where the formulation was presented in Li and Faltinsen (2012). Our calculation (not presented) showed a non-negligible contribution of the drag force to the floater, where the results are within the same order of magnitude as the Froude–Krylov force. This indicates a potentially significant contribution to wave-frequency viscous wave excitation loads for the floater's vertical flexible modes. Whether there is a viscous surge excitation load, or coupling with the floater's vertical flexible modes that causes the nonlinear surge excitation load needs a dedicated future study.

4. Conclusions

We investigated a scaled fabric membrane cage model. Model tests in regular wave conditions were performed with a half-spherical fabric membrane cage with a flexible floater under a range of incident wave periods and steepnesses. The first harmonic component of the floater and bag motions time series were analyzed. A rigid body motion analysis was performed using a linear frequency-domain code WAMIT, and the results were used to compare and analyze the first harmonic floater motions measured in the model tests.

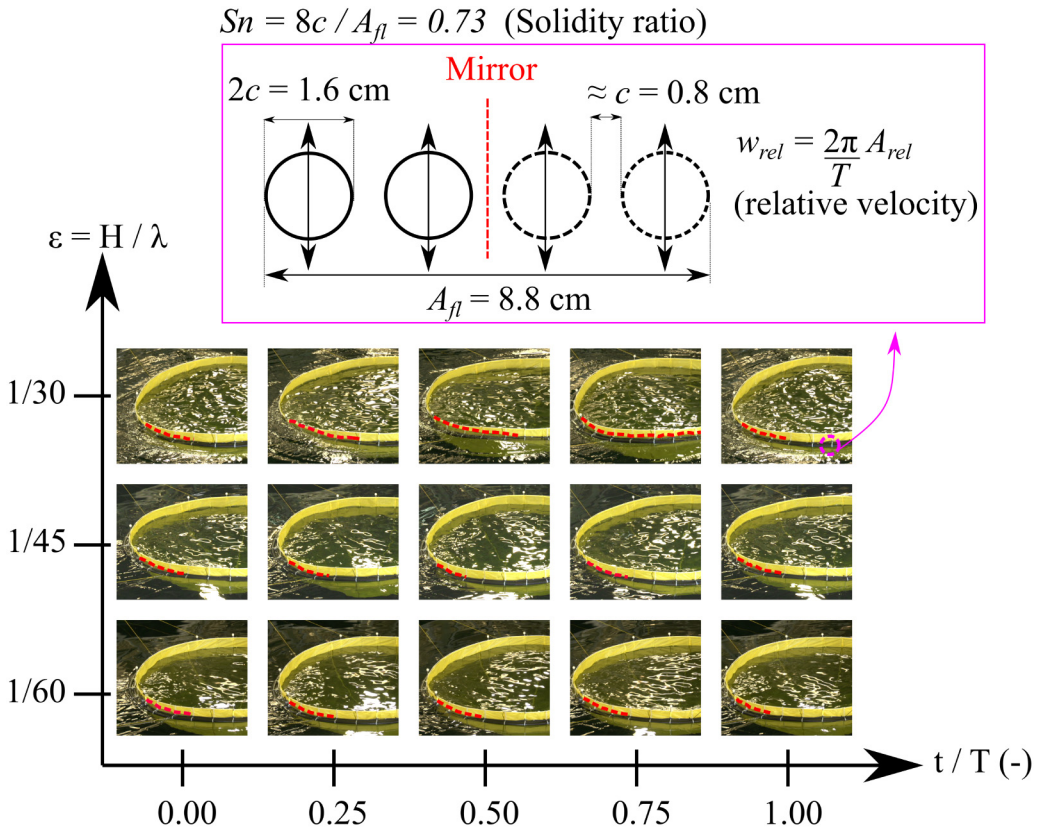

Fig. 14. Video snapshots of the floater's fore part from the tests at nondimensional wavelength $\lambda/D_{bag} = 1.11$ (see also Video 2). The incident wave direction is from left to right, where the drawn red lines are the visually observed free surface at the top of the floater. The snapshots for each test cover one period oscillation. In addition, definition used to estimate the two-dimensional drag force on the floater is given in the upper portion of the figure, where the equal distance between the cross-section of the floater was assumed to be c.

One of the observed features of the fabric membrane cage was a set-down phenomenon in which floater motion measurement showed that the cage model oscillates with a non-zero mean value in heave. The set-down magnitude increases with increasing incident wave period and steepness. Possible candidates are mean heave force due to the exterior flow problem, and coupling with the bag flexible modes. The latter might explain the observed set-down dependency on wave period and steepness, as the bag cannot transmit these forces to the floater due to its negligible compressive stiffness. The set-down may challenge the cage's maintenance of internal water volume integrity and the bag pretension; both are critical for the operational aspects of a fabric membrane cage in the sea.

The other observed phenomenon was a wavelike bag motion, a nearly periodic propagating fabric motion that originates from the bag's attachment to the floater and travels down to the bag bottom. The bag wave has a significant effect on the dynamics of the bag bottom, where the measured acceleration time series indicated the presence of snap loads. Snap loads can be an issue for the strength and fatigue of the fabric material. The first harmonic component of the bag motion was also analyzed, and the results show a high dependency of the bag motion amplitude on the incident wave period and steepness. Over the tested period range, the bag motion amplitudes near the free surface zone are mostly higher than in the other parts. However, at the vicinity of the heave natural period of the rigid cage $\lambda/D_{bag} = 3.02$, high bag bottom motion amplitudes were observed.

A third main feature was clear wave amplitude-dependent surge RAOs. Candidates are discussed, such as viscous drag loads on the floater, and coupling with the floater's vertical flexible modes, but a future dedicated study is needed to clarify the reasons. In addition, the measured rigid floater modes were compared with the numerical results from WAMIT. The rigid cage model was assumed in WAMIT calculation; hence, the bag and floater flexible modes were not considered. Several discrepancies between experiment and WAMIT results were apparent, which emphasizes the significance of modeling the cage's flexible modes. In other words, it is, as expected, inappropriate to assume a rigid body when performing hydrodynamic analysis of a fabric membrane cage. The first logical step would be to study the linear problem numerically, and the two-dimensional formulation presented in Strand and Faltinsen (2019) should be extended to three-dimensions. A further step would be to consider the sloshing and membrane geometric nonlinearity, as the latter was found to be important even for relatively small membrane deformation (Phadke and Cheung, 2003). If breaking waves

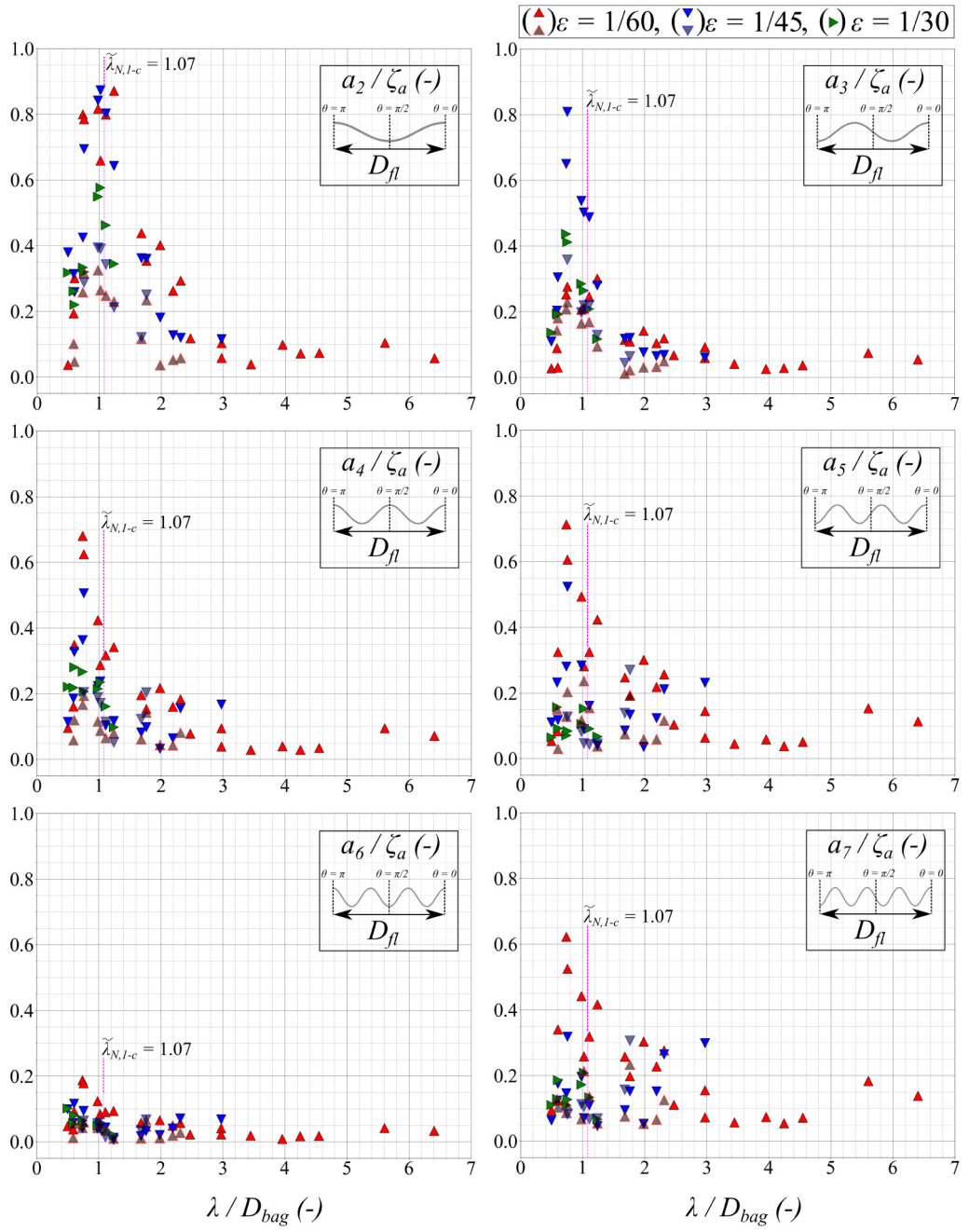

Fig. 15. The first six vertical flexible modes RAOs of the floater.

do not occur inside the cage, the nonlinear multimodal method described in Faltinsen and Timokha (2009) can be used to investigate sloshing nonlinear effects, such as swirling and chaos.

CRediT authorship contribution statement

Muhammad Mukhlas: Conceptualization, Methodology, Software, Validation, Formal Analysis, Investigation, Data curation, Writing – original draft, Writing – review & editing, Visualization. **Pål Furset Lader:** Conceptualization, Methodology, Investigation, Writing – review & editing, Supervision. **David Kristiansen:** Conceptualization, Methodology, Investigation, Writing – review & editing, Supervision. **Trygve Kristiansen:** Conceptualization, Writing – review & editing, Supervision. **Motoyasu Kanazawa:** Methodology, Software.

Declaration of competing interest

The authors declare that they have no known competing financial interests or personal relationships that could have appeared to influence the work reported in this paper.

Acknowledgments

This work was financed by the Research Council of Norway through the project Safe operation of CLOSED aquaculture CAGES in WAVES (Grant no. 268402) and by the Norwegian Seafood Research Fund through the project Sjøegenskaper og forankring til flytende lukkede oppdrettsanlegg (Grant no. 901287). The authors thank the anonymous reviewers for their valuable comments.

Appendix A. Supplementary data

Supplementary material related to this article can be found online at https://doi.org/10.1016/j.jfluidstructs.2021.103353.

References

Bradski, G., 2000. The OpenCV library. Dr. Dobb's J. Softw. Tools 25 (11), 120–125.
Broderick, L.L., Jenkins, C.H., 1993. Experimental investigation of fluid-filled membrane breakwaters. J. Waterw. Port Coast. Ocean Eng. 119 (6), 639–656. http://dx.doi.org/10.1061/(ASCE)0733-950X(1993)119:6(639).
Broderick, L., Leonard, J., 1992. Nonlinear water-wave structure interaction. Comput. Struct. 44 (4), 837–842. http://dx.doi.org/10.1016/0045-7949(92)90469-G.
Broderick, L., Leonard, J., 1995. Nonlinear response of membranes to ocean waves using boundary and finite elements. Ocean Eng. 22 (7), 731–745. http://dx.doi.org/10.1016/0029-8018(95)00009-A.
Cho, I.H., Kim, M.H., 1998. Interactions of a horizontal flexible membrane with oblique incident waves. J. Fluid Mech. 367, 139–161. http://dx.doi.org/10.1017/S0022112098001499.
Faltinsen, O.M., Shen, Y., 2018. Wave and current effects on floating fish farms. J. Mar. Sci. Appl. 17 (3), 284–296. http://dx.doi.org/10.1007/s11804-018-0033-5.
Faltinsen, O.M., Timokha, A.N., 2009. Sloshing. Cambridge University Press.
Hawthorne, W.R., 1961. The early development of the dracone flexible barge. Proc. Inst. Mech. Eng. 175 (1), 52–83. http://dx.doi.org/10.1243/PIME_PROC_1961_175_011_02.
Ibrahim, R.A., 2006. Liquid Sloshing Dynamics Theory and Applications. Cambridge University Press.
Kee, S.T., Kim, M.H., 1997. Flexible membrane wave barrier. II: floating/submerged buoy-membrane system. J. Waterw. Port Coast. Ocean Eng. 123 (2), 82–90. http://dx.doi.org/10.1061/(ASCE)0733-950X(1997)123:2(82).
Kim, M.H., Edge, B.L., Kee, S.T., Zhang, L., 1996. Performance evaluation of buoy-membrane wave barriers. In: 25th International Conference on Coastal Engineering. Florida. pp. 2087–2100. http://dx.doi.org/10.1061/9780784402429.162.
Kim, M.H., Kee, S.T., 1996. Flexible membrane wave barrier. I: analytic and numerical solutions. J. Waterw. Port Coast. Ocean Eng. 122 (1), 46–53. http://dx.doi.org/10.1061/(ASCE)0733-950X(1996)122:1(46).
Kristiansen, D., Endresen, P.C., Lader, P., Su, B., Volent, Z., Aksnes, V., 2018a. SJØFLO: Sjøegenskaper Og Forankring Til Flytende Lukkede Oppdrettsanlegg [Seakeeping Behavior and Mooring Forces of Floating Closed Fish Cages]. Technical Report 2018:00191, SINTEF Ocean.
Kristiansen, T., Faltinsen, O.M., 2012. Modelling of current loads on aquaculture net cages. J. Fluids Struct. 34, 218–235. http://dx.doi.org/10.1016/j.jfluidstructs.2012.04.001.
Kristiansen, D., Lader, P., Endresen, P.C., Aksnes, V., 2018b. Numerical and experimental study on the seakeeping behavior of floating closed rigid fish cages. In: Proceedings of the ASME 2018 37th International Conference on Ocean, Offshore and Arctic Engineering, Vol. Volume 6: Ocean Space Utilization. American Society of Mechanical Engineers, Madrid, http://dx.doi.org/10.1115/OMAE2018-77254.
Kristiansen, D., Su, B., Volent, Z., 2018c. Numerical and experimental study on the drainage and collapse of a floating flexible bag structure. J. Fluids Struct. 83, 429–447. http://dx.doi.org/10.1016/j.jfluidstructs.2018.09.013.
Lader, P., Fredriksson, D.W., Volent, Z., DeCew, J., Rosten, T., Strand, I.M., 2015. Drag forces on, and deformation of, closed flexible bags. J. Offshore Mech. Arct. Eng. 137 (041202), http://dx.doi.org/10.1115/1.4030629.
Lader, P., Fredriksson, D.W., Volent, Z., DeCew, J., Rosten, T., Strand, I.M., 2017. Wave response of closed flexible bags. J. Offshore Mech. Arct. Eng. 139 (051301), http://dx.doi.org/10.1115/1.4036676.
Lee, W., Lo, E.Y., 2002. Surface-penetrating flexible membrane wave barriers of finite draft. Ocean Eng. 29 (14), 1781–1804. http://dx.doi.org/10.1016/S0029-8018(02)00007-0.
Li, P., Faltinsen, O.M., 2012. Wave-induced vertical response of an elastic circular collar of a floating fish farm. In: 10th International Conference on Hydrodynamics. St. Petersburg.
Lo, E.Y.M., 2000. Performance of a flexible membrane wave barrier of a finite vertical extent. Coast. Eng. J. 42 (2), 237–251. http://dx.doi.org/10.1142/S0578563400000110.
Løland, G., Aarsnes, J.V., 1994. Fabric as construction material for marine applications. In: Proceedings of the International Conference on Hydroelasticity in Marine Technolgy. Trondheim, Norway. pp. 275–286.
Mciver, P., 1989. Sloshing frequencies for cylindrical and spherical containers filled to an arbitrary depth. J. Fluid Mech. 201 (1), 243. http://dx.doi.org/10.1017/S0022112089000923.
Newland, D.E., 2011. Mechanical Vibration Analysis and Computation. Dover Publications.
Newman, J., 2005. Wave effects on vessels with internal tanks. In: 20th International Workshop on Water Waves and Floating Bodies. Spitsbergen, Norway.
Nilsen, A., Hagen, Ø., Johnsen, C.A., Prytz, H., Zhou, B., Nielsen, K.V., Bjørnevik, M., 2019. The importance of exercise: increased water velocity improves growth of Atlantic salmon in closed cages. Aquaculture 501, 537–546. http://dx.doi.org/10.1016/j.aquaculture.2018.09.057.
Nilsen, A., Nielsen, K.V., Biering, E., Bergheim, A., 2017. Effective protection against sea lice during the production of Atlantic salmon in floating enclosures. Aquaculture 466, 41–50. http://dx.doi.org/10.1016/j.aquaculture.2016.09.009.

NS9415, 2009. Marine Fish Farms-Requirements for Site Survey, Risk Analyses, Design, Dimensioning, Production, Installation and Operation: Norwegian standard, SN/K 509. Technical Report.

Ohyama, T., Tanaka, M., Kiyokawa, T., Uda, T., Murai, Y., 1989. Transmission and reflection characteristics of waves over a submerged flexible mound. Coast. Eng. Japan 32 (1), 53–68. http://dx.doi.org/10.1080/05785634.1989.11924504.

Phadke, A.C., Cheung, K.F., 1999. Response of bottom-mounted fluid-filled membrane in gravity waves. J. Waterw. Port Coast. Ocean Eng. 125 (6), 294–303. http://dx.doi.org/10.1061/(ASCE)0733-950X(1999)125:6(294).

Phadke, A.C., Cheung, K.F., 2003. Nonlinear response of fluid-filled membrane in gravity waves. J. Eng. Mech. 129 (7), 739–750. http://dx.doi.org/10.1061/(ASCE)0733-9399(2003)129:7(739).

Rognebakke, O.F., Faltinsen, O.M., 2003. Coupling of sloshing and ship motions. J. Ship Res. 47 (3), 208–221. http://dx.doi.org/10.5957/jsr.2003.47.3.208.

Solaas, F., Rudi, H., Berg, A., Tvinnereim, K., 1993. Floating fish farms with bag pens. In: First International Conference Fish Farming Technology. Trondheim, Norway. pp. 317–323.

Strand, I.M., 2018. Sea Loads on Closed Flexible Fish Cages (Doctoral thesis). Norwegian University of Science and Technology, Trondheim, Norway.

Strand, I.M., Faltinsen, O.M., 2017. Linear sloshing in a 2D rectangular tank with a flexible sidewall. J. Fluids Struct. 73, 70–81. http://dx.doi.org/10.1016/j.jfluidstructs.2017.06.005.

Strand, I.M., Faltinsen, O.M., 2019. Linear wave response of a 2D closed flexible fish cage. J. Fluids Struct. 87, 58–83. http://dx.doi.org/10.1016/j.jfluidstructs.2019.03.005.

Strand, I.M., Faltinsen, O.M., 2020. Linear wave-induced dynamic structural stress analysis of a 2D semi-flexible closed fish cage. J. Fluids Struct. 94, 102909. http://dx.doi.org/10.1016/j.jfluidstructs.2020.102909.

Strand, I.M., Sørensen, A.J., Lader, P., Volent, Z., 2013. Modelling of drag forces on a closed flexible fish cage. In: 9th IFAC Conference on Control Applications in Marine Systems, Vol. 46. Osaka, Japan. pp. 340–345. http://dx.doi.org/10.3182/20130918-4-JP-3022.00014.

Strand, I.M., Sørensen, A.J., Volent, Z., 2014. Closed flexible fish cages: modelling and control of deformations. In: Proceedings of the ASME 2014 33rd International Conference on Ocean, Offshore and Arctic Engineering, Vol. Volume 8A: Ocean Engineering. American Society of Mechanical Engineers, San Francisco, http://dx.doi.org/10.1115/OMAE2014-23059.

Strand, I., Sørensen, A., Volent, Z., Lader, P., 2016. Experimental study of current forces and deformations on a half ellipsoidal closed flexible fish cage. J. Fluids Struct. 65, 108–120. http://dx.doi.org/10.1016/j.jfluidstructs.2016.05.011.

Tan, Y., Shao, Y., Read, R., 2019. Coupled motion and sloshing analysis of a rigid cylindrical closed fish cage in regular waves. In: Proceedings of the ASME 2019 38th International Conference on Ocean, Offshore and Arctic Engineering, Vol. Volume 6: Ocean Space Utilization. Glasgow. http://dx.doi.org/10.1115/OMAE2019-96002.

Tanaka, M., Ohyama, T., Kiyokawa, T., Uda, T., Omata, A., Characteristics of wave dissipation by flexible submerged breakwater and utility of the device. In: 23rd International Conference on Coastal Engineering. Venice. pp. 1613–1624. http://dx.doi.org/10.1061/9780872629332.122.

Tanaka, M., Ohyama, T., Kiyokawa, T., Uda, T., Ornata, A., 1990. Wave control by flexible underwater mound. In: Offshore Technology Conference. Houston. http://dx.doi.org/10.4043/6405-MS.

Thompson, G.O., Sollitt, C.K., McDougal, W.G., Bender, W.R., 1992. Flexible membrane wave barrier. In: Civil Engineering in the Oceans V : Proceedings of the International Conference. American Society of Civil Engineers, Texas, USA, pp. 129–148.

Tsarau, A., Lugni, C., Lucarelli, A., Kristiansen, D., Lader, P., 2021. Sloshing in a rotating liquid inside a closed sea cage for fish farming. Phys. Fluids 33 (3), 037114. http://dx.doi.org/10.1063/5.0037408.

Zhao, R., 1995. A complete linear theory for a two-dimensional floating and liquid-filled membrane structure in waves. J. Fluids Struct. 9 (8), 937–956. http://dx.doi.org/10.1006/jfls.1995.1053.

Zhao, R., Aarsnes, J.V., 1998. Numerical and experimental studies of a floating and liquid-filled membrane structure in waves. Ocean Eng. 25 (9), 753–765. http://dx.doi.org/10.1016/S0029-8018(97)00013-9.

Zhao, R., Triantafyllou, M., 1994. Hydroelastic analyses of a long flexible tube in waves. In: Proceedings of the International Conference on Hydroelasticity in Marine Technolgy. Trondheim, Norway. pp. 287–300.